2011

Study of the Added Mass of Cylinders and Spheres

Shelagh Fackrell
University of Windsor

Follow this and additional works at: https://scholar.uwindsor.ca/etd

STUDY OF THE ADDED MASS OF CYLINDERS AND SPHERES

By

Shelagh A. Fackrell

A Dissertation

Submitted to the Faculty of Graduate Studies

Through Mechanical, Automotive and Materials Engineering

In partial fulfillment of the requirements for the Degree of Doctor of Philosophy

at the University of Windsor

Windsor, Ontario, Canada

2011

STUDY OF THE ADDED MASS OF CYLINDERS AND SPHERES

By:

Shelagh A.Fackrell

Approved by:

_____
Dr. J. A. McCorquodale, External Examiner
Civil and Environmental Engineering Department,
University of New Orleans

_____
Dr. R. Balachandar, External Department Reader
Civil and Environmental Engineering Department,
University of Windsor

_____
Dr. D. Ting, Internal Department Reader
Mechanical, Automotive and Materials Engineering Department,
University of Windsor

_____
Dr. A. Fartaj, Internal Department Reader
Mechanical, Automotive and Materials Engineering Department,
University of Windsor

_____
Dr. G.W. Rankin, Advisor
Mechanical, Automotive and Materials Engineering Department,
University of Windsor

_____
Dr. Z. Pasek, Chair
University of Windsor

Author's Declaration of Originality

I hereby certify that I am the sole author of this thesis and that no part of this thesis has been published or submitted for publication.

I certify that, to the best of my knowledge, my thesis does not infringe upon anyone's copyright nor violate any proprietary rights and that any ideas, techniques, quotations, or any other material from the work of other people included in my thesis, published or otherwise, are fully acknowledged in accordance with the standard referencing practices. Furthermore, to the extent that I have included copyrighted material that surpasses the bounds of fair dealing within the meaning of the Canada Copyright Act, I certify that I have obtained a written permission from the copyright owner(s) to include such material(s) in my thesis and have included copies of such copyright clearances to my appendix.

I declare that this is a true copy of my thesis, including any final revisions, as approved by my thesis committee and the Graduate Studies office, and that this thesis has not been submitted for a higher degree to any other University or Institution

Abstract

The added mass for cylinders and spheres is examined for unidirectional constant acceleration.

In the case of cylinders, a numerical model is developed to determine the forces acting on the cylinder. The results of the model are compared to published experimental results and demonstrated to be a reasonable representation of the forces of an accelerating fluid acting on a stationary cylinder. This model is then used to investigate the effect of a constant non-zero velocity before the constant acceleration portion of the flow. Two different non-zero initial velocities are used as well as three different constant unidirectional accelerations and three different diameters. All sets of numerical experiments are shown to produce results that correlated very well when presented in terms of dimensionless forces and dimensionless distance. Two methods are presented for splitting the total force into unsteady drag and added mass components. The first method is based on the linear form of the equation that relates the dimensionless force, added mass, unsteady viscous drag and the dimensionless displacement. The slope includes the unsteady drag coefficient and the y-intercept includes the added mass coefficient. The second method, the Optimized Cubic Spline Method (OCSM), uses cubic splines to approximate the added mass coefficient and the unsteady drag coefficient variation with dimensionless distance. The parameters are optimized using the method of least squares. Both methods are compared with the experimental results. The OCSM produces better results therefore it is applied to the numerical experiment results.

The added mass coefficient for the initial portion of the acceleration of a sphere is studied experimentally using a high speed camera to determine the displacement of the sphere and subsequently the acceleration of the sphere. From the acceleration data and a mathematical model of the process, the dimensionless force on the sphere is calculated. The added mass is then determined using two approaches. For the first case the viscous drag is neglected and in the second case viscous drag is included by applying the OCSM. For small values of dimensionless distance, both methods produce added mass values close to those predicted by potential flow theory.

Dedication

"前人栽树，后人乘凉"

"One generation plants the trees, and another gets the shade"

Chinese Proverb

This dissertation is dedicated to

Linton, Nicholas and Akira.

As well as

Mom and Dad.

Acknowledgements

I would like to take this opportunity to thank my advisor, Dr. Gary W. Rankin, for his support, knowledge and guidance. His understanding and patience have been invaluable through this whole process.

I would also like to thank Andy Jenner for his help and his wonderful advice that saved both time and money. A thank you should also go to Kohei Fukuda who always seemed to be walking by when I needed an assistant to help me do the actual experiments. I give thanks to my fellow PhD student Mehrdad Shademan who was sent just in time for me to benefit from his experience in CFD.

I would also like to thank Dr. William Altenhof for letting me use his high speed camera. Without the use of his equipment I would not have been able to complete my research.

Table of Contents

List of Figures

List of Tables

Nomenclature

a acceleration

b y intercept (equation of a line)

C dimensionless force

C_{cal} calculated value of the dimensionless force

C_D unsteady drag coefficient

C_M added mass coefficient

C_{meas} measured value of the dimensionless force

D_o reference diameter = 0.0254 m

d diameter

$d_0 - d_4$ values of the y axis for each knot for the unsteady drag coefficient curve

F   force

F_{rel} force relative to the beginning of acceleration

F_0 force at the beginning of acceleration

$f''(x_i)$ second order derivative at x^{th} position

$f(x_i)$ function at x^{th} position

L length of cylinder

M mass

m slope of a line

M_{add} added mass

$M_{add,the}$ theoretical added mass

$m_0 - m_4$ values of the y axis for each knot for the added mass coefficient curve

s displacement

s_0 displacement relative to the beginning of acceleration

s_i displacement at the ith data point

t time

t_i time at the ith data point

V velocity

V_{rel} velocity relative to the beginning of acceleration

V_o velocity at the beginning of acceleration

y^+ dimensionless wall distance

Greek Letters

ρ density

u_τ friction velocity

y_P distance from the closest point P to the wall
μ viscosity
ϵ error

Chapter 1 - Introduction

The force exerted by a fluid on a bluff body has been of interest to researchers and designers for many years. The complexity of the research has ranged from the simple static case to complicated accelerating cases. In terms of general interactions between a bluff body and the surrounding fluid, the simplest form occurs when both the body and the fluid are not moving. The interaction in this case is only a pressure force but no shear force; the net effect is the buoyancy force. The interaction becomes more complicated when either the bluff body or the fluid moves at a steady rate. In this situation, there is an additional force due to the viscous shear. This combines with the pressure forces that are different from those for the static case and results in a drag force along the direction of the flow and in the opposite direction. The interaction is even further complicated by the addition of unsteady velocity in either the fluid or the body. When considering an unsteady velocity flow situation the fluid particles around the object generate yet another force. The inertia associated with the fluid particles change the pressure and shear distributions when compared to the steady flow case. This additional force is, in reality, a fluid inertia force.

Initial work in this area was done by Du Buat[1]. Du Buat performed a series of experiments on spheres accelerating in water and air, in which he noticed that the forces could not be accurately described by Newton's Second Law,

$$F = (M)a. \tag{1.1}$$

In the case of an object accelerating through a stationary media the missing force is the inertia force of the fluid being accelerated out of the way of the moving object. In the case of an accelerating fluid over a stationary object it represents the difference between the inertia force of the fluid with and without the presence of the object[2].

Du Buat found that the inertial force was proportional to the acceleration. This means that for an object of mass M, undergoing acceleration, a, another mass, M_{add}, needed to be "added" in order to better account for the forces, i.e.:

$$F = (M + M_{add})a. \tag{1.2}$$

The addition of an "added mass" term has become a standard approach to handling this additional force.

1.1 Background/Literature Review

One of the earliest methods of theoretically estimating the added mass of an object was the use of potential flow theory which does not take into account the effect of viscosity or compressibility. There are several text books such as those by Yih[3], Lamb[4] and Birkhoff[5] which contain a theoretical development of the added mass for basic geometries. There is also a large amount of work that has been done on a wide variety of more complicated geometries as documented by Kennard[6], Brennen[2], Patton[7] and Keulegan and Carpenter[8].

When considering flow over a complicated geometry, the problem becomes extremely complex. The complication is due to the fact that added mass forces can arise in one direction due to motion in a different direction (translational or rotational). For an arbitrary motion, an object has six degrees of freedom; three translational and three rotational. For each component of acceleration of the object there is a relationship to the inertial forces imposed on the fluid by this acceleration, i.e. acceleration in one direction may cause an inertial force in another direction. This relationship is usually expressed in the form of a 6x6 added mass tensor. There are possibly 36 different scalar values that are required to describe the added mass. Thankfully, it is not usually necessary to deal with all 36 elements. Through proper choice of the origin and use of geometric symmetry the number of elements can usually be reduced to something more reasonable. This is one of the main reasons for the extensive use of cylinders and spheres in the literature in this field of study, including the present work.

The assumptions of inviscid, irrotational and incompressible flow raise the question of how reasonable the approximation is and in what range it can be used for a viscous flow. The major affect that viscosity has on the flow over bluff bodies is the

formation of a wake which is known to greatly affect the drag and inertial forces acting on the object. According to Sarpkaya and Isaacson[9], the added mass will vary with the shape and volume of the wake as well as its rate of change. The treatment of viscosity can be included in theoretical work with varying degrees of success. Sarpkaya[10] placed vortices in his potential flow solution in order to simulate the effect of viscosity. The use of potential flow to determine the added mass has also been extended to include more complicated flow dynamics such as that by Villaggio[11] for deformable cylinders.

When dealing with real fluids there are two main approaches used to treat the drag and added mass forces on the bodies. Some researchers, such as Bird[12], use a pseudo-steady drag (the unsteady drag is taken as the steady state drag at the corresponding instantaneous velocity) along with a constant (potential flow value) for the added mass. Others, such as Sarpkaya[10], Sarpkaya and Garrison[13] and Garrison[14] show that the unsteady drag force (proportional to the square of the instantaneous velocity) differs from the pseudo-steady value and the added mass force (proportional to acceleration) also changes with time.

The use of a pseudo-steady drag and constant Potential flow value for added mass has been shown, by Bird[12], to require an additional Basset history force to completely account for all effects of acceleration. The history force is the force associated with the change in the flow pattern over time. When an object moves from one position to another, the flow field does not instantaneously adjust. This concept was first introduced by Basset[15, 16]. The mathematical nature of the force does not allow easy application to practical situations. It is also unknown as to what range of motion this term is applicable. Sarpkaya's view that there are just two forces, drag and the inertia, which both change with time, is a simpler approach that inherently accounts for the Basset history term [12].

For the special case of a sinusoidal relative motion between the flow and object, it can be mathematically shown that the history term is zero. This was a concept introduced by Morison et al[17]. Morison was interested in the forces exerted by waves on submerged cylindrical objects. The Morison equation utilizes the principle that the drag is proportional to the square of velocity while the added mass is proportional to the acceleration at discrete points of time.

1.1.1 Experimentally/Numerically Determining Added Mass

Historically, two distinctly different approaches have been developed for experimentally determining the added mass of an object. These will be referred to as the indirect force measurement approach and direct force measurement approach. These methods will be discussed more fully in the following paragraphs in connection with their application to cylinders and spheres.

The first of two techniques in the category of the indirect force measurement approach is most suited for determining the added mass of groups of irregular objects such as rubble mounds with high blockage effect such as the work presented by Hannoura[18] and Hannoura and McCorquodale[19, 20]. This approach uses the head loss across the objects by measuring the pressure difference across the objects as well as the velocity upstream of the object. The pressure difference can be used to determine the head loss over the test section. The pressure difference across the objects for accelerated flow is compared to the steady flow pressure difference across the same set of objects. The difference between the steady and unsteady resistance is considered as the acceleration head for the object and is proportional to the added mass of the objects. Although this is a good technique when trying to determine the added mass of a group of objects, it is most useful when the majority of the test area is blocked, hence a large pressure difference can be measured. This type of measurement also requires that the velocity profile before and after the object be fairly uniform. For a cylinder or sphere in a similar flow situation the wake is not uniform which would require pressure measurements at more than one place along the velocity profile. For these reasons this type of measurement is not considered for use in the current study.

The second indirect force measurement approach makes use of the velocity field and its derivatives to determine the forces acting on an object. This technique is of interest because of recent developments in Particle Image Velocimetry (PIV) which makes it possible to determine the instantaneous velocity at a large number of points throughout a flow field. Noca[21] and Noca et al[22] derived three different equations for the force on an object completely contained within a region of fluid in terms of the

velocities and derivatives of velocity at different locations within the region. His "impulse" method required information on the instantaneous velocity and derivative (vorticity) field throughout the volume. The "momentum" method required the instantaneous velocity field while his "flux" method only required instantaneous velocity information on the boundary enclosing the region. He conducted experiments on accelerating circular cylinders which indicated a self-consistency in the results among the three methods. However, he was not able to obtain independent force measurements and could not determine the accuracy of the methods.

Although the main focus of his work is the derivation of a term used to measure the force, a small section was included which specified the equations needed to calculate the added mass in terms of the velocity field. Although showing promise in two-dimensional flow situations, the technique would be difficult, if not impossible to apply in three-dimensional cases such as spheres. Hence, no further consideration is given to velocity field methods in this dissertation.

The direct force method is the traditional approach to determining added mass. It consists of measuring the components of the total force acting on the object subjected to an accelerated motion with the use of a force transducer and then splitting the total force into the appropriate components (i.e. drag and added mass force). It is common practice to accelerate the fluid and have the object stationary in added mass research as this is closer to the scenario encountered in offshore structure design. This, however, presents a problem when comparing the results to an accelerating object in a stationary fluid. When the fluid is accelerated, as opposed to the object, there is an added pressure that the moving fluid exerts on the object. Determining the fluid's inertia force requires that this be taken into account. The added pressure of the accelerated fluid will result in an "added mass" that consists of the actual added mass plus the mass of the fluid displaced by the object. The added mass coefficient (actual added mass divided by the theoretical added mass) for a circular cylinder is two for an inviscid, irrotational flow in which the fluid is accelerating and one for an inviscid, irrotational flow in which the fluid is stationary and the object is accelerating.

Researchers also have chosen to study simple motions since it is very difficult, if not impossible, to find a correlation between a truly arbitrary acceleration and the

resulting added mass. The two most common simple motions are sinusoidal oscillation and unidirectional translation.

In the case of sinusoidal motion of the object (or the fluid) the total force on the object is measured and then split into its components; added mass and drag. The drag is assumed to be proportional to the square of the velocity component and the added mass is assumed to be proportional to the acceleration component of the measured force calculated at the discrete positions of the prescribed sinusoidal motion. For sinusoidal motion the Basset history term is mathematically shown to be equal to zero which yields a more manageable relationship. This is the approach that Morison et al [17] took when determining the added mass for cylinders in a sinusoidal wave. The data were analyzed and separated into drag and added mass by looking at the measured forces at two phases in the cycle, one when the velocity is zero and one when the acceleration is zero. Morison et al [17] were able to show that during the phase of the cycle when velocity is zero, the force represents the inertial component of the total force. During the phase when the acceleration is zero the force represents the unsteady drag of the force. Many experimentalists, such as Keulegan and Carpenter [8], have modified the original Morison equation in order to have a better representation of actual forces. Keulegan and Carpenter[8] added a remainder function to account for the difference between the computed values and observed values. Other researchers have also used a similar approach for oscillating cylinders as well as spheres with a variety of techniques to account for any discrepancy between calculated and observed values in a variety of flow situations[23-42]. One of the other reasons for the popularity of conducting experimental work using an oscillating cylinder/sphere is that sinusoidal motion is a common approximation for modeling wave forces. This becomes important for the application of designing offshore structures, which is the most common application requiring accurate added mass information. Some problems associated with this method are: difficulty in measuring the instantaneous velocity and acceleration instead of simply deriving them, several flow regimes exist based on the combinations of experimental parameters chosen (i.e. the Reynold's number based on the frequency, the Keulegan-Carpenter number) which are complicated to quantify, and results are not readily transferable to general motion.

It can be argued that the case of unidirectional acceleration gives results that are more easily transferable to general motion due to the fact that any general variation can always be separated into small steps of constant acceleration.

There is a relatively limited amount of research that has been reported on unidirectional acceleration for both cylinders and spheres. The most comprehensive body of work for cylinders is that done by Sarpkaya[10], Sarpkaya and Garrison[13] and Garrison[14]. It includes data on unidirectional, constant acceleration of fluid over a stationary cylinder in terms of a dimensionless force and a dimensionless distance. The experiments included several different diameters and accelerations which showed excellent correlation. This set of experiments also used flow visualization to determine the size and strength of the vortices in the wake region. These measurements were then applied to the formulations originally developed by Sarpkaya [10] which allowed the force to be split into the unsteady drag and the inertia components. There are a few other variations of this research: Keim[43] experimented with cylinders of different lengths but did not separate the resulting force into drag and inertia components; Sarpkaya[44] accelerated cylinders and flat plates to a constant velocity (added mass was constant); and McLain[45] and McLain and Rock[46] experimented on an underwater manipulator, determining the added mass using a vortex technique. Bird[12] also performed experiments for unidirectional accelerating and decelerating cylinders, however the acceleration was not a constant. The scenarios in this set of experiments included acceleration from rest, deceleration to rest, acceleration from one constant velocity to another and reversal of flow. The added mass was assumed to be the theoretical value derived from potential flow while the drag was calculated using pseudo-steady drag. The remainder of the measured force was considered to be the history force.

The most comprehensive work for spheres undergoing unidirectional constant acceleration was that of Moorman[47]. Moorman used a photographic method for determining the time and distance required for a sphere to reach terminal velocity. In order to determine an appropriate equation to predict this particular aspect of accelerated flow Moorman used a constant potential flow value of added mass. There were several different variations of this set of experiments including Odar [48] who added a simple

7

harmonic component to the fluid and Hamilton and Courtney[49] who studied the effect of a solid boundary on the accelerating sphere.

Engineers and designers are depending more on numerical approaches in order to reduce the need for expensive experimental apparatus. This is a growing area of research in the field of unsteady flow, but there is still a limited amount of material that is specifically directed toward the added mass of an object in a unidirectional, constant acceleration. The work that is the most closely related to the present study is the work by Wang and Dalton [50] for impulsively started flow over cylinders .

Numerical studies that are directly comparable to Moorman's experimental results are also available. Ferreira and Chhabra [51], Chang and Yen[52] and Guo[53] were interested in determining the time and distance required for a sphere to reach terminal velocity and they used Moorman's experimental results for comparison. In these papers there is no focus on the beginning of the flow and determining the added mass is not the main goal.

The issue of splitting the total force into the drag and inertia terms has been resolved in two fundamentally different ways. The first method, employed by Bird [12], uses the pseudo-steady drag and the theoretical (potential flow) value of the added mass. These two terms are added together and then subtracted from the total force in order to determine the value of the Basset history term. The assumption made in this first method is that the instantaneous velocity governs the drag as if it were in a steady flow situation. The second method splits the force into an unsteady drag (different than the value at the same steady velocity) plus an unsteady added mass force, as done by Sarpkaya and Garrison[13]. The assumptions made in this method are: drag is proportional to the square of the velocity, added mass is proportional to the acceleration and the total force is simply a linear summation of the drag and inertial components. One of the other important contributions by Sarpkaya and Garrison[13] is the development of a dimensionless force (C) which is the measured force in the direction of the flow divided by fluid inertia force (M_{add} x acceleration). This form of the dimensionless force uses the acceleration instead of the conventional velocity and is shown to be the dimensionless group that is required to collapse the data The method employed by Sarpkaya and Garrison[13] has the least restrictive assumptions concerning the values of the

coefficients. This method has the inherent problem of identifying the coefficients. The equation relates the added mass and drag coefficients to the force, but there is only one equation for two unknowns. Sarpkaya[9] attempted to solve this problem by assuming the coefficients were constant over a short period of time. Thus a system of two equations and two unknowns were solved, however the results were very noisy. McLain[45] and McLain and Rock[46] developed a method of curve fitting using a polynomial cubic spline with non-linear optimization for the case of an underwater manipulator oscillating in a fluid. The technique helped to overcome the problem with noise.

1.2 Summary of Literature Review

A review of the literature regarding added mass and the resulting inertial force indicates that considerable effort has been made, over many years, to identify ideal (potential) flow values for a variety of shaped objects. Spheres and circular cylinders have been the focus of most of the research papers in the literature due to the single added mass coefficient required as a result of symmetry in addition to their important practical applications. In practical usage these potential flow theory values of added mass continue to be applied in the equations used to describe the forces acting on objects in general acceleration situations in real fluids in spite of their questionable accuracy. The Basset force term, which is required in this case, is often neglected.

Experimental research is limited to simple types of relative motion of the object and the fluid due to the complexity involved with handling the general acceleration variation in real fluids. The most common simple types of motion are sinusoidal and constant unidirectional acceleration. The sinusoidal variation has direct application to wave forces of water on offshore structures. Research on this topic is quite well advanced but is limited to the application mentioned.

There is a relatively limited amount of research regarding constant unidirectional acceleration of flow over circular cylinders. It has been found that the added mass values determined using potential flow theory accurately describe the values found during the initial period of motion of an object starting from rest [12, 54]. This is surprising in that

the Reynolds number of the flow is extremely small during that time which would tend to imply that viscous effects are important, however, during that time the relative flow between the fluid and object, and hence the shear stress, has not had time to establish. The case of a constant relative acceleration from an initially non-zero relative velocity needs further study. It is clear that the usual thought process involved with steady flows cannot be applied when considering unsteady flow situations.

Although there has been research work reported on spheres falling from rest, most of these studies were concerned with the time required to reach terminal velocity. A fundamental study, similar to that of Garrison[14] and Sarpkaya and Garrison[13] for the circular cylinder, is missing in the literature.

1.3 Objectives of this Study

The overall objectives of the present study are to extend the state of the art in the field of added mass in the following ways; to extend the research in the area of unidirectional constant acceleration of an initially stationary fluid over a stationary circular cylinder to include flows with a small initial velocity (Re < 40) and to provide new experimental data for that of a sphere falling from rest with a constant acceleration in a stationary medium. This work, therefore, is limited to applications where the Reynolds number is quite small. An application example in the case, of the circular cylinder is the approximation to insect motion by Kikuchi and Mochizuki[55] while the acceleration of bubbles in a liquid as described by Brennen[56] is a good example of low Reynolds flows associated with spheres. The specific objectives in each of these cases are given in the following.

1.3.1 Study of Cylinders

1) To develop a numerical model to simulate the forces exerted by a fluid, which is accelerated over a stationary cylinder.

2) To investigate the case of a circular cylinder subjected to an initially steady flow followed by a constant unidirectional acceleration using computational fluid dynamic techniques and compare with the potential flow values. The initial steady state values are limited to the laminar flow regime.

3) To develop an analysis technique similar to the dimensionless technique of Sarpkaya's to separate the drag force and the force due to inertia (or added mass) in the case mentioned above.

1.3.2 Study of Spheres

The experiments presented in this dissertation explore the added mass values at the beginning of the accelerated flow immediately after a sphere is released from rest.

1) To experimentally study spheres of different density, falling in a stationary fluid to determine the added mass at different values of acceleration.

2) To develop a dimensionless technique similar to Sarpkaya's that can be applied to the sphere undergoing constant acceleration.

3) To determine the added mass of a sphere using simplifying assumptions and compare with the potential flow values.

Chapter 2 - Numerical Investigation of the Added Mass of Cylinders Subjected to a Constant Acceleration after an Initially Steady Flow

The numerical study presented in this section involves a determination of the added mass of a circular cylinder subjected to an initially constant velocity followed by constant acceleration. A numerical model is developed for this purpose and used to conduct numerical experiments. The error that results in using the potential flow value of added mass is of particular interest.

The chapter begins with a description of the governing equations that are being solved numerically. This is followed by a description of the physical geometry being modeled and its computational approximation. A discussion of the boundary conditions and the details involved in obtaining the numerical solution using the commercial software package Fluent are given next. Considerations made in determining the final form and parameters for the model are then presented for the case of a constant acceleration from a condition of rest. The results are then validated by comparison with existing experimental results for this case.

Numerical experiments for determining the fluid forces acting on a circular cylinder experiencing a constant velocity followed by a constant acceleration are then presented. The results are presented in a dimensionless form which is an extension of that used by Sarpkaya[9].

Finally, two methods of separating the total dimensionless force into the drag and inertial components are presented, evaluated using existing experimental results and then applied to the results of the current numerical experiment.

2.1 Governing Equations

The commercial software package used to solve the acceleration of fluid over a stationary cylinder is Fluent 6.3.26. The pressure based solver is used because it was originally developed for low velocity incompressible flow, which gives it an advantage in the current flow situation; incompressible flow which begins from rest[57]. PISO (Pressure-Implicit with Splitting of Operators) is a pressure based segregated algorithm that is highly recommended for transient flow[57]. Segregated solvers will solve for each individual fluid parameter for each cell using the pressure and mass flux across each cell face then move on to the next fluid variable. After all the variables are solved with the current pressure and mass flux across each cell face, the solution is checked for convergence. If convergence is not satisfied then the process is repeated.

The basic governing equations are the conservation of mass

$$\frac{\partial \rho}{\partial t} + \nabla \cdot \rho u_i = 0, \tag{2.1}$$

and the conservation of momentum,

$$\frac{\partial}{\partial t}(\rho u_i) + \nabla \cdot (\rho u_i u_j) = \nabla p + \nabla(\bar{\bar{\tau}}) + \rho \vec{g}. \tag{2.2}$$

where ρ is the density, u is the component of the velocity in the ith and j^{th} direction, p is the pressure, $\bar{\bar{\tau}}$ is the stress tensor and g is the gravitational acceleration.

These equations apply to laminar flow, for which there are no fluctuating components superimposed on the mean velocities or pressures. However, turbulent flow is characterized by fluctuations in the velocities and pressures at each point. Fluent uses Reynolds Averaged Navier Stokes (RANS) equations in order to reduce the computational expense of trying to resolve the entire range of turbulence fluctuations. The instantaneous velocities used in Equation 2.1 and Equation 2.2 are replaced by a turbulent velocity that is composed of a mean and a fluctuating velocity,

$$u_i = \bar{u}_i + u_i'$$ (2.3)

where $\bar{u}_i$ is the mean component and u_i' is the fluctuating component. Substituting the mean and fluctuating velocities for the velocities in Equation 2.1 and 2.2 and averaging gives

$$\frac{\partial \rho}{\partial t} + \nabla \cdot \rho \bar{u}_i = 0$$ (2.4)

and

$$\frac{\partial}{\partial t}(\rho \bar{u}_i) + \frac{\partial}{\partial x_j}(\rho \bar{u}_i \bar{u}_j)$$
$$= \frac{\partial}{\partial x_i}\bar{p} + \frac{\partial}{\partial x_j}\left[\mu\left(\frac{\partial \bar{u}_i}{\partial x_j} + \frac{\partial \bar{u}_j}{\partial x_i} - \frac{2}{3}\delta_{ij}\frac{\partial \bar{u}_l}{\partial x_l}\right)\right]$$
$$+ \frac{\partial}{\partial x_j}\left(-\rho\overline{u_i'u_j'}\right)$$ (2.5)

where $-\rho\overline{u_i'u_j'}$ are the Reynold's stress terms. The Reynold's stress terms represent the mean transport of momentum caused by the turbulent velocity fluctuations. These additional Reynold's stresses cause a closure problem i.e. in the case of incompressible flow, there are four equations and ten unknowns (four mean variables and six Reynold's stress terms). In order to overcome this, Fluent uses what is called the Boussinesq approach where the Reynold's stresses are assumed to be related to the mean flow velocity gradients with the same form as in the laminar flow case, except that a turbulent viscosity is used instead of the fluid viscosity. The closure problem, hence reduces to specifying a relation for the turbulent viscosity. This is accomplished using turbulence models which involve the solution of one or more model transport equations which may be either algebraic or differential equations, the details of which are provided in the literature [52]. Many of the models also assume that the Reynold's stresses are isotropic, which is not true in general. The turbulent transfer equations involve coefficients which have been empirically determined. No references that deal with the effect that acceleration has on the coefficients could be found in the literature and hence, these coefficients are assumed to applicable to accelerated flow.

2.2 Physical Geometry, Computational Domain and Mesh

The numerical model simulates a water tunnel in which cylinders of varying sizes (0.0127 m -0.0254 m in diameter) are placed. The water is initially allowed to achieve a steady downward flow and then is accelerated. The special case of zero initial velocity is also considered in order to evaluate the model using existing experimental data.

A complete and unobstructed velocity field is required to gather the necessary data for the determination of added mass and hence, a domain is chosen slightly larger than that normally recommended for bluff body simulations. The distances from the inlet and outlet to the cylinder are chosen in order to reduce the influence of these boundaries on the velocity field as shown in Figure 2.1. An upstream dimension of 20 diameters is considered an adequate distance to allow for the natural adjustment of the flow approaching the object from that given at the inlet boundary. A downstream dimension of 60 diameters is considered adequate to include the steady flow wake effects caused by the cylinder. Since the cylinder and the wall were both assigned a no-slip boundary condition a distance of 12 diameters from the centre of the cylinder to the wall was considered sufficient in order to avoid any effects of the wall on the cylinder. This dimension is larger than that used experimentally by Garrison[14] and Sarpkaya and Garrison[13] in order to produce an accurate steady state result for the value of the drag force. Use of the original experimental dimensions was investigated and found not to have an influence on the solution for simulations that have a constant uniform acceleration starting from rest. However when the flow was started from an initial velocity other than rest the experimental dimensions caused inaccurate forces to be calculated for the initial, steady state portion of the flow.
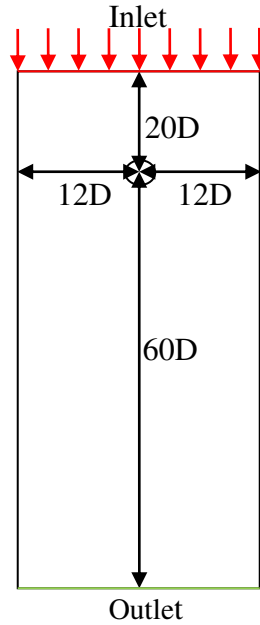
Figure 2.1: Schematic of the physical flow field.

Both the sides of the flow region as well as the cylinder are defined as walls. The side walls are placed sufficiently far away from the cylinder as to not interfere with the flow around it. It is expected, however, that there will be very high gradients around the cylinder and in the wake region; hence a finer mesh is desired in these areas. In order to realize the higher density meshes and still have a manageable mesh size, the fluid region is divided into nine regions as shown in Figure 2.2. The region surrounding the cylinder has the highest density mesh. The mesh density then decreases as it moves away from the cylinder. All grids considered consisted of a structured mesh attached to the cylinder wall that extended at least 10% of the cylinder diameter into the flow field. The mesh attached to the structured mesh was an unstructured mesh that had a high density in the wake region in order to resolve any gradients that are present at the edge of the wake.

Special attention must be paid to the boundary layer around the cylinder. Since this is a flow with an adverse pressure gradient, the near wall region must be resolved adequately to resolve the laminar region extremely close to the wall. This requires that the y+ value be close to one. The y+ value is defined as

$$y^+ = \frac{\rho u_\tau y_P}{\mu} \tag{2.6}$$

16

where u_τ is the friction velocity, y_p is the distance from the node point, P, closest to the cylinder wall, ρ is the density of the fluid and μ is the viscosity of the fluid at point P. The proper range of y+ for the cylinder wall is achieved using the Fluent y+ adaptation function. This function splits, in half, the cells that do not meet the criteria in height and width. This effectively doubles the number of nodes around the cylinder.
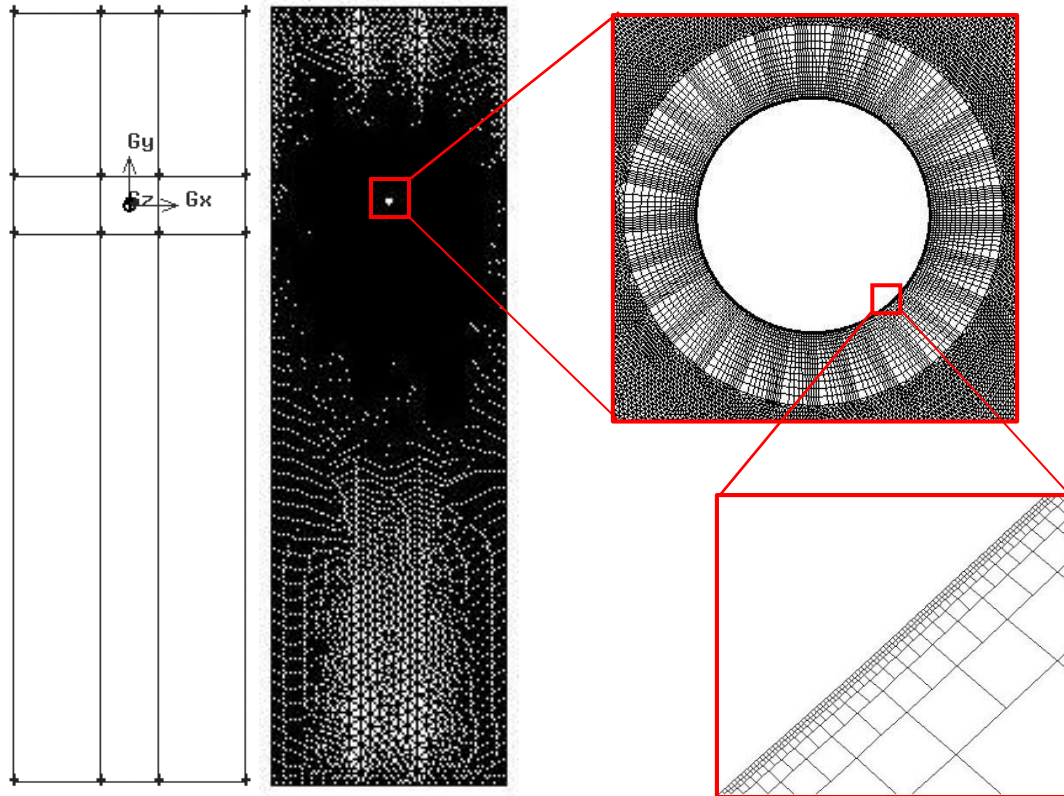
Figure 2.2: Mesh of solution region.

2.3 Boundary Condition

The vertical walls as well as the cylinder surface are set to the no-slip boundary condition. The inlet boundary condition is defined by a User Defined Function (UDF) (See Appendix A). For purposes of model testing the UDF is a constant acceleration in the direction normal to the inlet boundary (-y direction) starting from an initial zero velocity. This UDF is modified for the numerical experiment section which is described later. The outlet is set to outflow which assumes zero gradients perpendicular to the

17

outlet. Since the outlet is a considerable distance from the cylinder, this is a reasonable assumption to make.

2.4 Numerical Aspects of the Model

According to the Fluent documentation [57] and Jones and Clarke[58] an appropriate turbulence model for a bluff body is the k-omega SST (Shear-Stress Transport) model due to its ability to handle the adverse pressure gradient that results in boundary layer separation. Since the entire model includes flow with a varying velocity over a wide range, the flow field could include both laminar and turbulent regions therefore the transitional flow option is used in the k-omega SST turbulence model.

Second order solvers are chosen for the Pressure, Momentum, Turbulent Kinetic Energy and Specific Energy dissipation equations. Quadratic Upstream Interpolation for Convective Kinetics (QUICK)[57] is also used since it is found to have negligible difference compared to other second order solvers. Pressure-Implicit with Splitting of Operators (PISO)[57] is used for the pressure-velocity coupling method since this is a transient flow situation. The under-relaxation factors used for the simulations can be found in Table 2.1.

	Under-Relaxation Factor
Pressure	0.3
Density	1
Body Force	1
Momentum	0.5
Turbulent Kinetic Energy	0.8
Specific Dissipation	0.8
Turbulent Viscosity	1

Table 2.1: Under-Relaxation Factors used in numerical simulations

Default settings are used for the convergence criterion except for the steady velocity simulations used in the numerical experiments. For steady velocity simulations a convergence criteria with a residual of 1e-6 is used.

2.5 Validation of Model and the Parameters

This section begins with a comparison of the different factors that affect the accuracy of the two-dimensional solution. These factors or parameters are selected to ensure that the model yields an accurate solution in a reasonable period of time.

2.5.1 Grid Convergence

In order to get an accurate simulation, the gradients around the cylinder must be resolved adequately. The most important factor in determining whether a grid is able to resolve the high gradients on the surface of the cylinder is the height of the first layer of cells next to the cylinder wall. Although a number of grid configurations are studied, three are chosen in order to demonstrate the important factors associated with a successful mesh. Table 2.2 gives more detailed information about the three meshes that are considered when determining grid convergence.

	1st Cell Height	Total No. of Cells	Nodes Around the Cylinder
Mesh 1	1.961e-6 m	178001	13775
Mesh 2	3.132e-6 m	206043	937
Mesh 3	3.924e-6 m	149666	9600

Table 2.2: Mesh information for grid convergence study.

It is critical that this first layer be very small, however this high level of mesh density does not need to extend throughout the whole flow field. The most effective way

19

of achieving this high mesh density near the surface and still have a manageable number of cells in the whole mesh is to use Fluent's mesh adaptation feature in order to have a resulting y+ value of approximately 1. This is the technique that is used in the simulations used in this case.
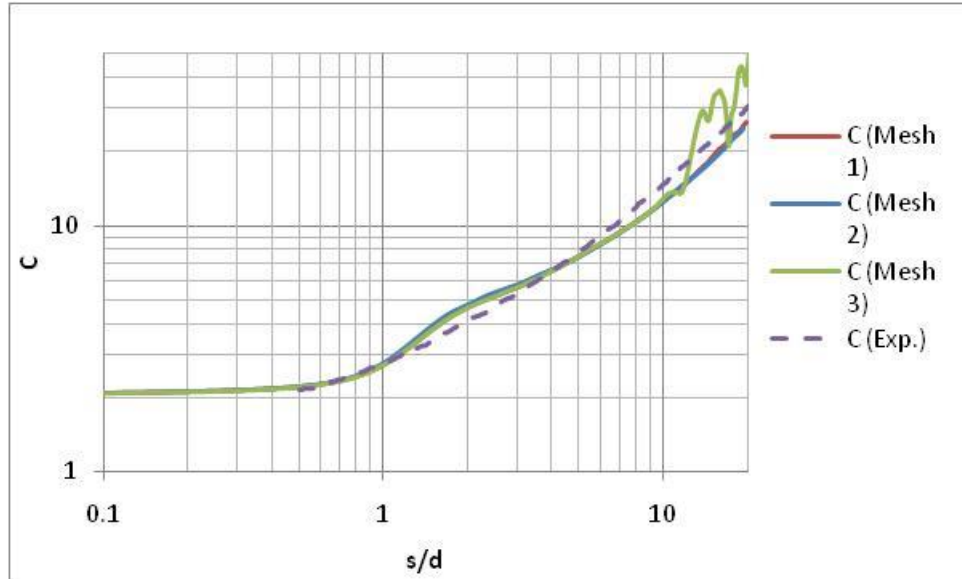
Figure 2.3: Comparison of different grid configurations (experimental data from Sarpkaya and Garrison [13]).

Figure 2.3 shows the dimensionless force (as described in Section 1.1.1) versus the dimensionless distance moved by the cylinder for the three different meshes compared to the experimental results from Sarpkaya and Garrison[13]. As can be seen from Figure 2.3 the case with the largest height of cell next to the cylinder boundary shows oscillation beginning at an s/d value of around 12. By decreasing the first cell height by approximately 1e-6 m (i.e. from 3.924e-6 m to 3.132e-6 m) the oscillation is delayed to values of s/d greater than 20 and hence do not appear on the graph. However, decreasing the first cell height by another 1e-6 m does not change the results. It is decided that the simulations use a first cell height of 2e-6 m to ensure the high velocity gradients are resolved.

It is also observed from Figure 2.3 that the number of cells around the cylinder is not a good indication of the reliability of the mesh. The cylinder with the least number of cells around the cylinder (Mesh 2) still performed well compared to the medium density mesh (Mesh 3). Although it had similar results to Mesh 2, the aspect ratio for Mesh 1 is

one whereas the aspect ratio for Mesh 2 is around 4. Mesh 1 is used in the remainder of the simulations.

It should be noted that there is a discrepancy between the numerical and experimental results in the form of a "hump" at lower values of s/d. This will be discussed in detail in Section 2.5.5.

2.5.2 Choice of Turbulence Model

Several turbulence models are available in Fluent 6.3.26 including Laminar, Spalart-Allmaras, k-epsilon, k-omega and RSS. As stated in Section 2.4, according to the literature[57, 58] the most appropriate model is the k-omega SST turbulence model. This is due to its superior treatment of the viscous near wall region in addition to accounting for the effects of stream-wise pressure gradients. The SST version also accounts for the transport of turbulent shear stresses. In addition, Fluent has incorporated a (transitional) low- Reynolds number version of this model which applies when fine grids are utilized. These features are important in accurately modeling the boundary layer separation process which is of paramount importance in obtaining good results for flow over bluff bodies. The other models are, however, considered here to verify their lack of applicability. In each case, all other conditions regarding the numerical model are kept constant except the turbulence model. Both the k-epsilon and the RSS models utilize the enhanced wall function which is used in the simulations for comparison. This allows the use of a wall function that can be more appropriately used for a near wall region that includes a consideration of a laminar sub-layer, buffer region, and fully-turbulent outer region. Since the transitional flow option is used for the k-omega model, the same guide lines as for the enhanced wall function apply. The inlet turbulence conditions are specified using a turbulence intensity and a turbulence length scale. The values of the turbulence intensity considered for the inlet boundary condition are 1%, 2% and 5%. A value of 10% for the turbulence intensity is considered very high and a value of 1% is generally considered low(from Fluent User's Manual[57], Section 7.2.2). Although several different values for these two conditions were tested there was little effect on the end result. The turbulence variables are set for the inlet boundary conditions which are

far enough away from the cylinder for any effects to have been dissipated by the time the flow reaches the cylinder. Another consideration is the difference in the turbulence from the beginning of the flow (at rest) and the end of the simulation (moderate turbulence). The value of the turbulent length scale was based on the recommended value as determined from the equation

$$l = 0.07L. \tag{2.7}$$

where l is the turbulent length scale and L is the characteristic length which in this case is the diameter of the cylinder.
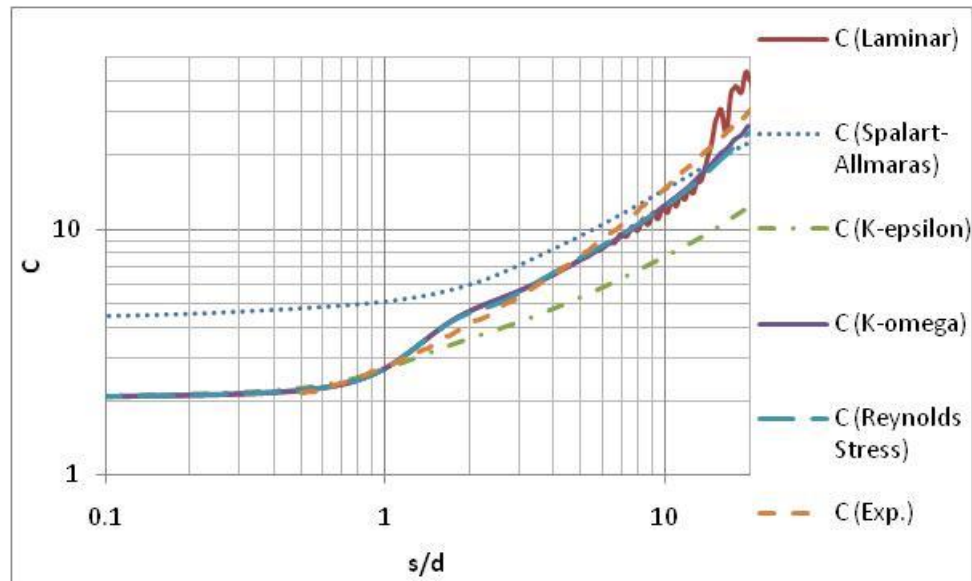
Figure 2.4: Comparison of different Fluent turbulence models (experimental data from Sarpkaya and Garrison [13]).

Figure 2.4 shows the dimensionless force results for the turbulence models tested as well as the experimental results for comparison. From Figure 2.4 several things can be observed about the different turbulence models. The laminar model shows the occurrence of vortex shedding very early on in the simulation while the others do not. The experimental results of Sarpkaya do not indicate such a vortex shedding (fluctuations in the force measurement) and hence this model is unrealistic. The k-epsilon model shows a much lower value of C than the other models and, therefore not desirable. Although the Spalart-Allmaras model seems to show similar results to the k-omega and Reynolds Stress models for higher values of s/d, the initial value of C is closer to five upon inspection. This is in disagreement with experimental results and theoretical results

so the use of this model is also discounted. The two remaining models, k-omega and Reynolds Stress, show excellent agreement with each other with only a slight difference at higher values of s/d (>18) and hence both are considered to be equally applicable. The Reynolds Stress model requires a longer computational time than the k-omega model, therefore the k-omega model is chosen as the turbulence model for the remainder of the simulations.

2.5.3 Time Step Independence

A 2D model with a first layer height of 2e-6 m, using a k-omega SST turbulence model is run with several different time steps in order to determine the optimal time step.
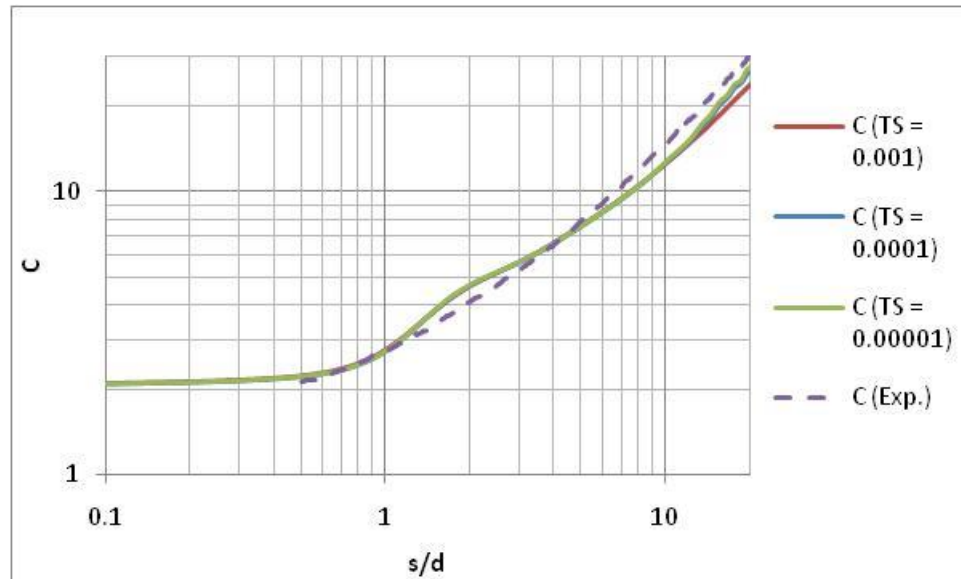
Figure 2.5: Comparison of different time steps (experimental data from Sarpkaya and Garrison [13]).

The time step is initially chosen such that the fluid, at its maximum velocity, does not pass through more than one cell boundary within the time step. This is determined to be approximately 0.0001 s. The time step is then decreased and increased from this value by a factor of 10 to determine if any change in the solution is apparent. As indicated in Figure 2.5, when the time step increases (0.001 s) the small oscillations are not present. This indicates that the time step is not sufficiently small to resolve this flow. However

when the time step is decreased (0.00001 s) there is little change to the solution. Therefore a time step of 0.0001 s is used for the remainder of the simulations.

2.5.4 Three-dimensional versus Two-dimensional Model Geometry

The computational time required for a two-dimensional numerical solution of the flow field is considerably less than that for a three-dimensional numerical solution simply because of the reduction in the number of cells that need to be determined. The important point to consider is whether the two-dimensional assumption reduces the accuracy of the solutions to an unacceptable level. In this regard, a comparison is made between solutions for a three-dimensional and a two-dimensional representation of the flow field in question.

The width and height of the fluid domain remain the same for both cases. The length of the cylinder (for three-dimensional case) is the same as the width of the fluid domain and the cylinder extends all the way to the end walls which are given the no slip boundary condition.   Similar to the two dimensional simulation, the three dimensional simulation uses y+ adaptation to produce the small first cell height that is required for an accurate solution.   In order to keep the number of nodes reasonable enough for a 12 CPU computer to complete a solution, the y+ is adapted in order to obtain a value of four which is still within the range suggested as acceptable by the Fluent User's Manual [57] and considerably reduces the number of nodes that are generated. The value of the acceleration is 9.81 m/s^2 and the boundary conditions as well as flow parameters (i.e. k-omega SST turbulence solver, time step of 0.0001secs, and relaxation factors as described in Table 2.1) are the same for both simulations.
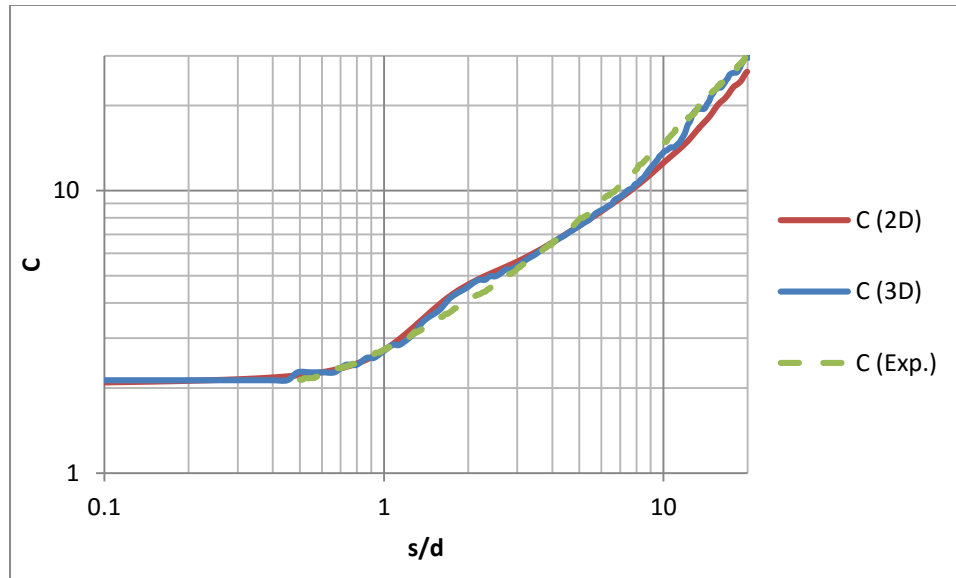
Figure 2.6: Comparison of three-dimensional and two dimensional simulation results (experimental data from Sarpkaya and Garrison [13]).

The results of this comparison are shown in Figure 2.6 and demonstrate that there is little difference between the two results for the lower values of s/d. For the range 0<s/d<9, the maximum difference between the two results is less than 6%. The maximum difference is 18.6% which occurs at s/d = 12.9. From Figure 2.6 it can be seen that the three dimensional simulation begins to oscillate due to early (pre-mature) onset of vortex shedding. This presents itself in the simulation data as a wave in the C value. The experimental data does not show this wave in the C data which suggests that the 2D simulation, which does not indicate the vortex shedding, is a closer representation of the experimental results. The maximum difference occurs when the oscillation for the three dimensional results is at a maximum compared with a two dimensional simulation that is not oscillating. The difference between the two simulations occurs at higher values of s/d, which is outside the range of interest for the remainder of the work, therefore no further modification done on the 3 dimension model to reduce the oscillations (i.e. reducing the y+ further). In terms of computational time a three dimensional simulation takes approximately 15 days with a computer with a Intel(R) Core™ i7 CPU x980@3.33GHz 3.33 GHz processor, 600 GB RAM and a 64-bit Operating System while the two dimensional simulation takes less than six hours on the same computer.

25

In the present study it is the time immediately after the acceleration begins that is of particular interest, therefore, it is important to have an accurate and efficient solution in the region 0<s/d<5. Hence, the use of 2D simulations can be justified in view of the drastically reduced simulation times with comparable accuracy.

2.5.5 Further Comparison of Numerical Model with Experimental Data

Having established grid independence, the appropriate turbulence model and the appropriate time step, the results will be compared to the experimental work of Garrison[14] and Sarpkaya and Garrison [13] over the range of s/d of interest. Although both curves in Figure 2.7 have been seen previously on various figures, it is advantageous to present them again in order to emphasis the results and aid in further discussion.
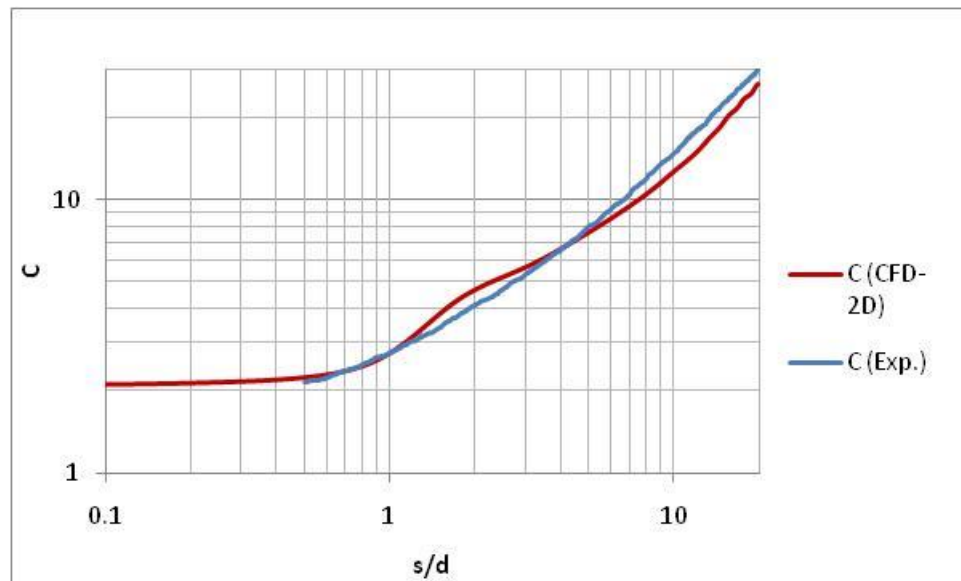
Figure 2.7: Comparison of experimental and numerical results (experimental data from Sarpkaya and Garrison [13]).

The comparison of the experimental work with the CFD work, presented in Figure 2.7, shows a reasonable agreement. It can be seen that there is a slight "hump" in the CFD results when compared to the experimental results for values of s/d in the range (1.3<s/d<4). It can also be seen that the CFD results do not compare as well as the value of s/d increases. This study focuses on the beginning of the accelerated flow (s/d<5) and

hence this is not considered to be a problem. The "hump", however, is an interesting phenomenon and will be investigated in more detail in the following paragraph.

Figure 2.8 shows the streamlines for various values of s/d throughout the duration of the "hump". Along with the streamline diagrams is a graph showing the numerical results (red line) and the experimental results (blue line) with a green square that indicates the position that corresponds to the streamline diagram. The third graph for each set is the y-wall shear stress of the cylinder with respect to the x position. This graph is used to determine the separation point. The shear stress changes from positive to negative when separation occurs. It should be noted that the shear stress also changes sign due to recirculation. The start of the "hump" does not coincide with the formation of the large vortices in the wake of the cylinder. It does, however, coincide with the formation of the smaller vortices located just after the separation points.

The streamline diagrams also include red arrows that indicate the approximate point of separation. It can be seen that the point of separation quickly recedes back to approximately 90º due to the formation of the smaller secondary vortices. When examining the experimental visualization results of Garrison[14], there does not seem to be a distinct set of secondary vortices at similar values of s/d. These results are consistent with the fact that the numerical results have a higher drag force. It appears that this is due to the premature recession of the separation point which in turn is due to the over estimation of the secondary vortex development in size and strength. The premature recession of the separation point increases the amount of drag on the cylinder, which in turn produces a higher force in the direction of the flow. This difference exists both in the two-dimensional as well as the three-dimensional solutions.

Another difference in the simulation compared to the experimental work is the difference in the slope at intermediate values of s/d. This may be due to the symmetry of the attached vortices. According to Sarpkaya and Garrison[13], asymmetry of the attached vortices occurs around an s/d value of 3. From Figure 2.8, however, there does not seem to be any asymmetry apparent for s/d values as high as four (Figure 2.8 f).
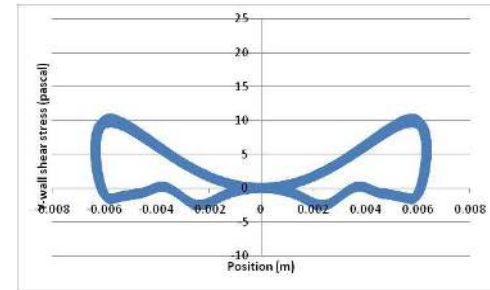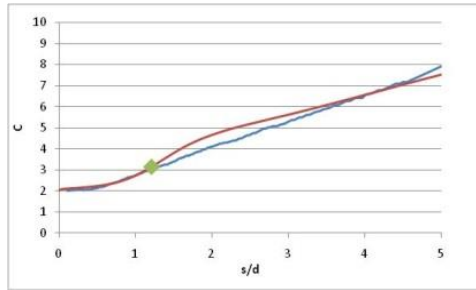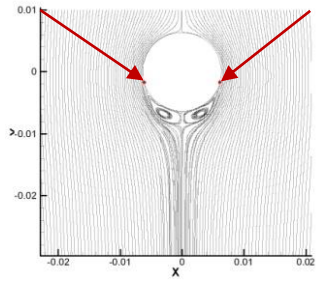
a) time = 0.056 s, s/d = 1.211, Separation =105.49^O from leading edge
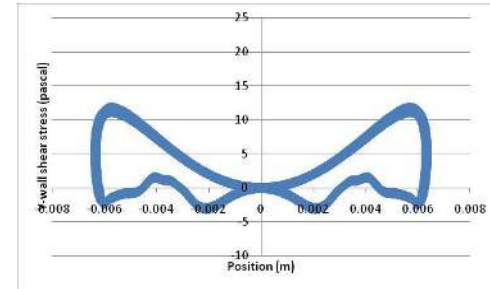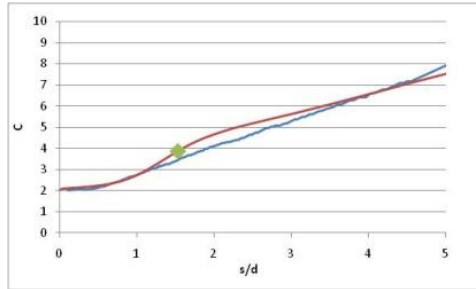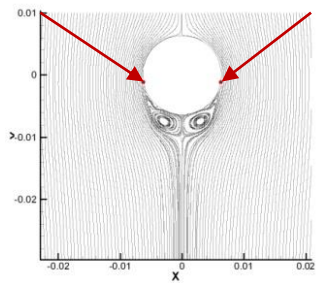
b) time = 0.063 s, s/d = 1.533, Separation = 100.31^O from leading edge
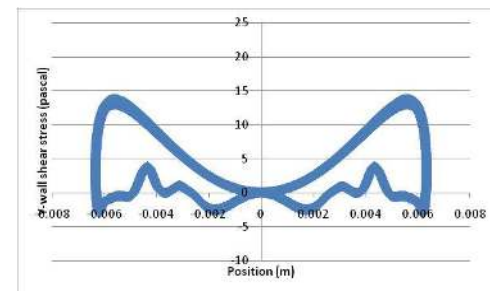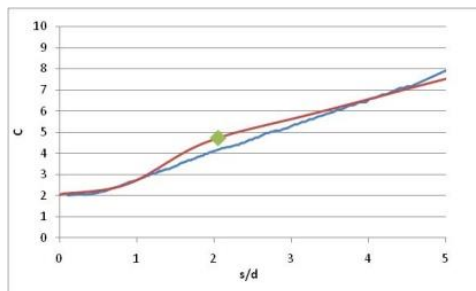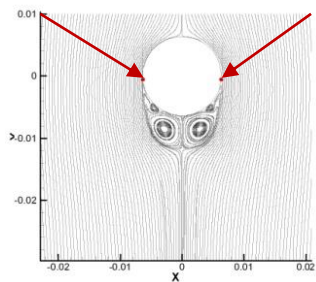
c) time = 0.073 s, s/d = 2.058, Separation = 95.06^O from leading edge

28
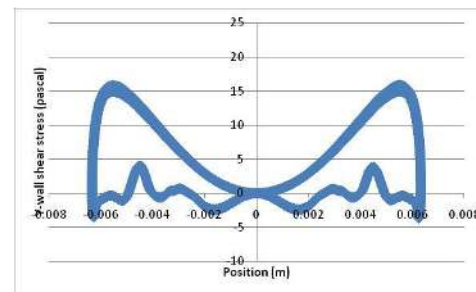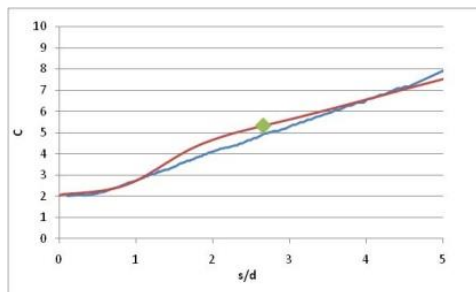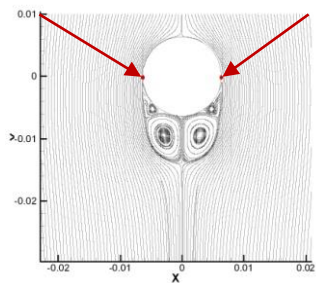
d) Time = 0.083 s, s/d = 2.661, Separation = 91.65^O from leading edge
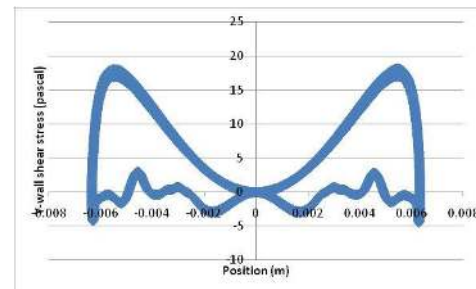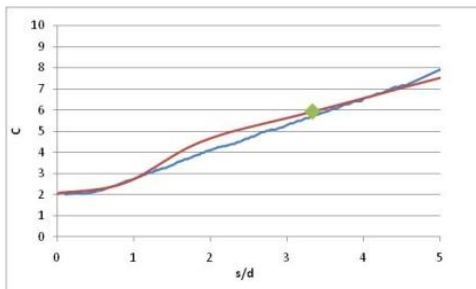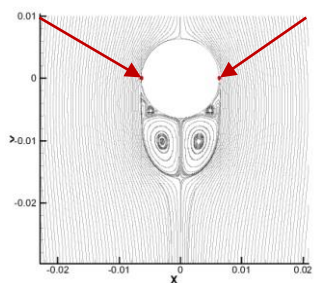
e) Time = 0.093 s, s/d = 3.340, Separation = 89.70^O from leading edge
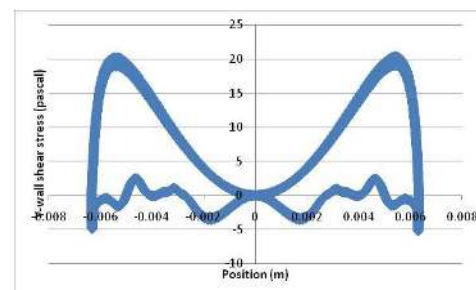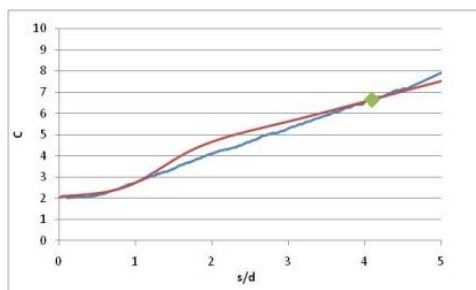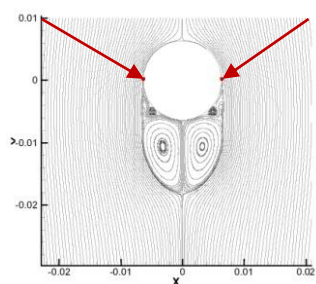
f) Time = 0.103 s, s/d = 4.097, Separation = 87.98^O from leading edge

Figure 2.8: Streamlines of numerical experiments for diameter = 0.0127 m at various times (first graph shows the value that corresponds to the diagram (green square), numerical results (red line) and experimental results from Sarpkaya and Garrison[13] (blue line), second graph shows the y-wall shear stress over the cylinder, red arrows indicate point of separation).

In order to further investigate possible reasons for the formation of the "hump" two additional geometries are studied. The first tank has width to diameter ratio twice as large as the original and the second has exactly the same geometry as that of Sarpkaya and Garrison[13] to see if blockage contributes to the differences. Figure 2.9 shows there is no difference between the solutions which demonstrates that there is no evidence that blockage effect is smoothing out the "hump" in the experimental results.
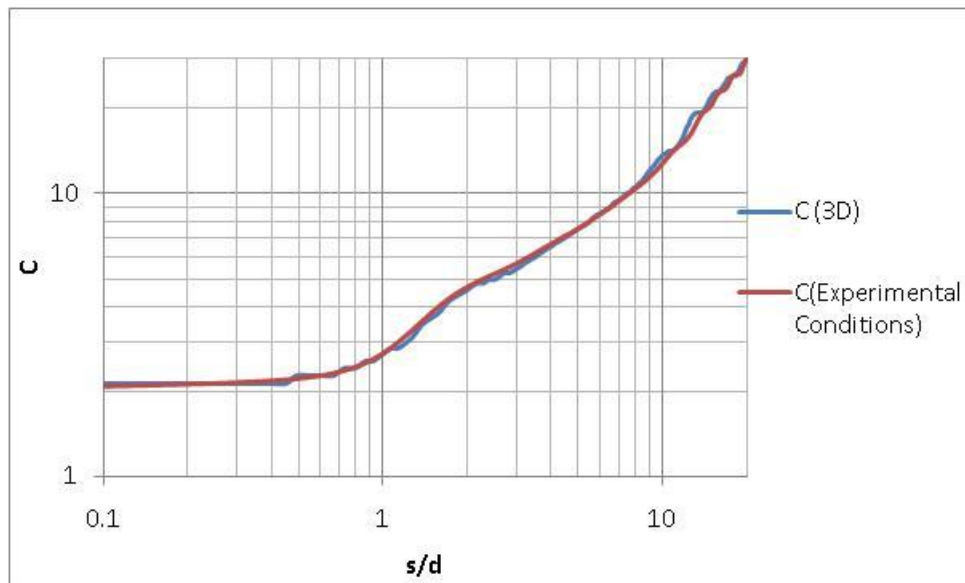
Figure 2.9: Comparison of 3D numerical simulation with 3D numerical simulation using physical parameters of experimental set up by Sarpkaya and Garrison[13].

2.6 Numerical Experiments

Now that the CFD methodology has been verified, it is possible to use it as a tool to perform numerical experiments which would have otherwise been very costly and physically difficult to perform. Another advantage to using CFD for this type of study is the ability to accurately determine the forces at very low values of s/d. It is difficult to obtain experimental data at the beginning of accelerated flow due to the small forces that are involved.

Most of the available work on added mass for unidirectional constant acceleration concerns an initially zero velocity. In addition to that condition, this investigation deals

with the flow situation that starts from a constant velocity, other than zero, then experiences a constant unidirectional acceleration.

The numerical experiments that are presented in the following sections are for the case of unidirectional, constant acceleration of fluid flowing over a stationary cylinder following a non-zero constant velocity of the fluid. The simulation is first run for a constant velocity of the fluid until convergence. The constant acceleration is then implemented. The solver used for the constant velocity portion of the simulation is also an unsteady solver to account for any unsteadiness that may develop in the wake. The residuals are set to 1e-6 for this portion of the simulation and the solution is considered to have converged when the measured C_D reaches a constant value. The C_D values obtained for a Reynolds number of 40 range from 1.77 to 1.89 where the experimental value is 1.8[59]. The C_D value obtained for a Reynolds number of 10 is 3.53 where the experimental value is 3.57[60]. The grid, turbulence mode and, time step are all the same for both the constant velocity and constant acceleration portions of the simulation. It should be mentioned that the Reynolds numbers are based on one cylinder diameter with the value of the constant velocity adjusted accordingly.

The following sections include a comparison of the results for the three different initial constant velocities followed by an acceleration of 9.81 m/s^2. Similar to Sarpkaya and Garrison[13], a comparison is made for a change in the acceleration, ranging from 2 m/s^2 to 9.81 m/s^2 while the initial velocity and the diameter of the cylinder remain constant. Finally, the diameter is adjusted in the range from 0.00635 m to 0.015875 m, while the initial velocity and the acceleration remain the same. The results of these numerical experiments will be presented non-dimensionally as described in the next section.

2.6.1 Equations for Cylinder Starting from Non-zero Constant Velocity

Garrison[14] and Sarpkaya and Garrison[13] found that regardless of the diameter of the cylinder or acceleration of the fluid, the data consistently correlated well when using the dimensionless variables C vs. s/d. A similar development can be made for

the case of a constant, unidirectional acceleration starting from non-zero constant velocity. These equations are developed in this section.

The total force acting on a cylinder can be separated into the drag and inertia forces for the case of acceleration from rest as indicated below.

$$F = C_D \rho \frac{V^2}{2} dL + C_M (M_{add}) a \,, \tag{2.8}$$

where F is the force action on the cylinder, C_D is the unsteady drag coefficient, ρ is the density, V is the velocity of the fluid, L is the length of the cylinder, C_M is the added mass coefficient, M_{add} is the added mass, and a is the acceleration.

For the case of the fluid undergoing an initial constant velocity a similar approach can be taken using quantities that are relative to the initial conditions, such as the Force (F) and the velocity (V) in the following form,

$$F_{rel} = C_D \rho \frac{V_{rel}^2}{2} dL + C_M (M_{add}) a, \tag{2.9}$$

where

$$F_{rel} = F - F_o, \tag{2.10}$$

$$M_{add} = \frac{\pi d^2 L}{4} \rho \,, \tag{2.11}$$

and

$$V_{rel} = V - V_o, \tag{2.12}$$

where F_o is the initial force exerted on the cylinder during the steady state portion of the flow and V_o is the velocity of the steady state portion of the flow.

Acceleration is also a relative term, however, it is rectilinear and the acceleration that is used for comparison (during the constant acceleration) is zero. Therefore it is simply referred to as the acceleration. Substituting Equation 2.10 and 2.11 into Equation 2.9 results in,

$$F - F_o = C_D \rho \frac{V_{rel}^2}{2} dL + C_M \left(\frac{\pi d^2 L}{4} \rho \right) a. \tag{2.13}$$

Dividing both sides of Equation 2.13 by the term $(\frac{\pi d^2 L}{4}\rho)a$, gives,

$$\frac{F - F_o}{\left(\frac{\pi d^2 L}{4}\rho\right)a} = \frac{C_D\rho\frac{V_{rel}^2}{2}dL}{\left(\frac{\pi d^2 L}{4}\rho\right)a} + C_M. \qquad (2.14)$$

Expressing Equation 2.14 per unit length and simplifying yields,

$$\frac{F - F_o}{\left(\frac{\pi d^2}{4}\rho\right)a} = \frac{2C_D V_{rel}^2}{(\pi d^2)a} + C_M \qquad (2.15)$$

In order to get Equation 2.15 in terms of s/d the equations for displacement and velocity in a constant unidirectional acceleration that does not start from rest, $V_o{\neq}0$ are required and shown below.

$$s = V_o t + \frac{1}{2}at^2. \qquad (2.16)$$

Rearranging Equation 2.16,

$$a = \frac{2}{t^2}(s - V_o t) \qquad (2.17)$$

where

$$s_{rel} = (s - V_o t) \qquad (2.18)$$

and

$$V = V_o + at. \qquad (2.19)$$

Substituting Equation 2.18 into Equation 2.17 gives,

$$a = \frac{2}{t^2}s_{rel}. \qquad (2.20)$$

Rearranging Equation 2.19 and substituting Equation 2.12 into it gives,

$$a = \frac{V - V_o}{t} = \frac{V_{rel}}{t} \tag{2.21}$$

Equating Equation 2.21 and Equation 2.20 gives a relationship between the relative velocity and the relative displacement as,

$$\frac{V_{rel}}{t} = a = \frac{2s_{rel}}{t^2}. \tag{2.22}$$

This can also be expressed as,

$$V_{rel} = \frac{2s_{rel}}{t}. \tag{2.23}$$

Substituting Equation 2.23 and Equation 2.20 into Equation 2.15 gives,

$$\frac{F - F_o}{\left(\frac{\pi d^2}{4}\rho\right)a} = \frac{2C_D \left(\frac{2s_{rel}}{t}\right)^2}{(\pi d^2)\left(\frac{2s_{rel}}{t^2}\right)} + C_M \tag{2.24}$$

Simplifying Equation 2.24 yields,

$$\frac{F - F_o}{\left(\frac{\pi d^2}{4}\rho\right)a} = C = C_D \frac{4}{\pi} \frac{s_{rel}}{d} + C_M \tag{2.25}$$

It can be seen that the equation is the same as that developed by Sarpkaya and Garrison[13] if the initial velocity and force are set to zero.

2.6.2 Results and Discussion for Cylinder Starting from Non-zero Constant Velocity

The first set of data presented is a comparison of the C values determined using different initial velocities. The initial velocity is chosen in order to have a resulting Reynolds number of 10 and 40 respectively, based on the diameter of the cylinder. The

34

results for three different initial velocities (including $V_{init} = 0$) are shown in Figure 2.10 along with the experimental results from Sarpkaya and Garrison[13].
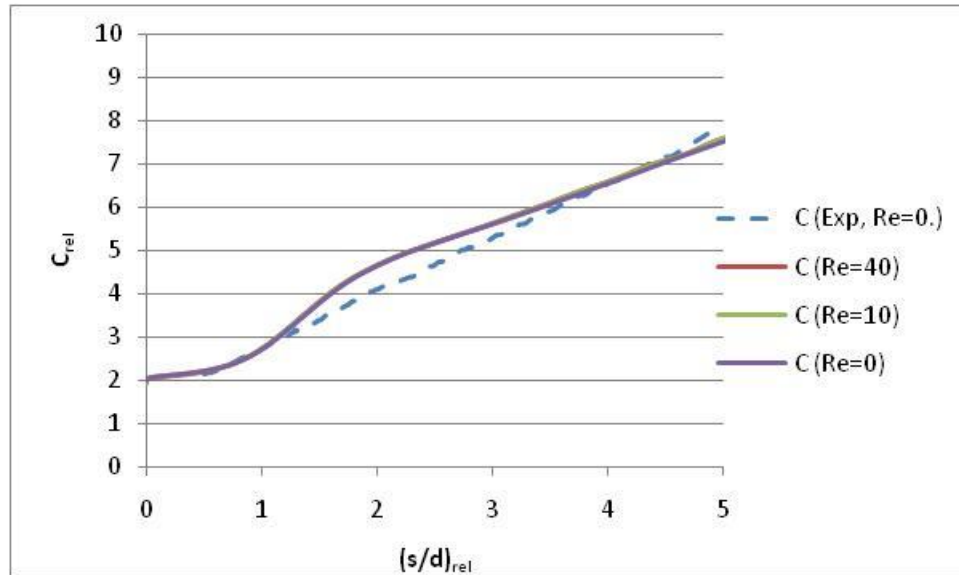
Figure 2.10: Numerical results for different initial velocities (experimental data from Sarpkaya and Garrison [13]).

As can be seen from Figure 2.10 the results are almost identical regardless of the initial velocity when plotted using relative values. The initial velocity does not seem to have any effect which is not what was expected.

The second set of numerical experiments consists of simulations with the same diameter and initial velocities but three different accelerations. The accelerations are presented in dimensionless form (a/g) with respect to gravitational acceleration (g).
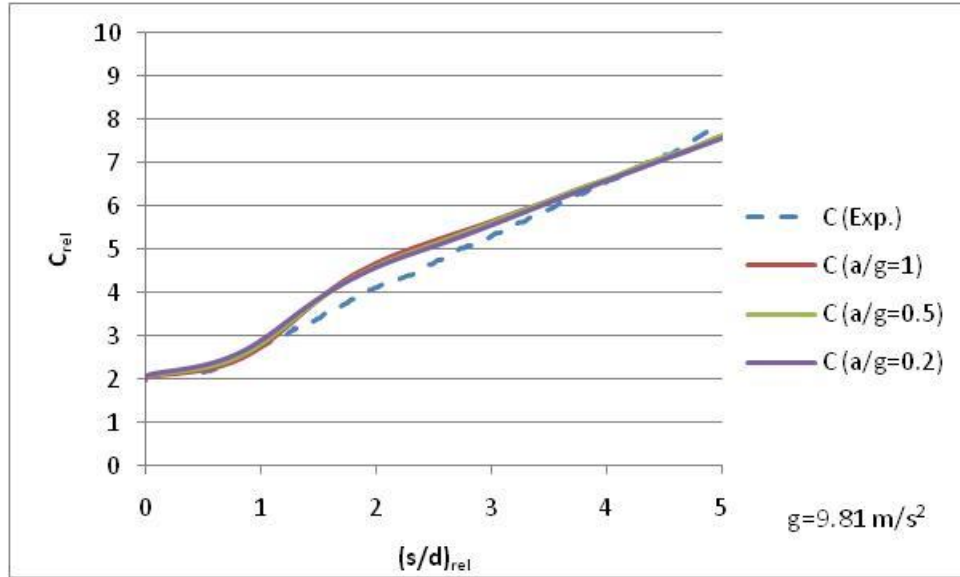
Figure 2.11: Numerical results for different accelerations (experimental data from Sarpkaya and Garrison [13]).

It can be seen from Figure 2.11 that the data correlate very well regardless of the acceleration of the cylinder. This implies that the dimensionless variables are effective in collapsing the data.

The third set of numerical experiments consists of the same initial velocities and accelerations but three different cylinder diameters.
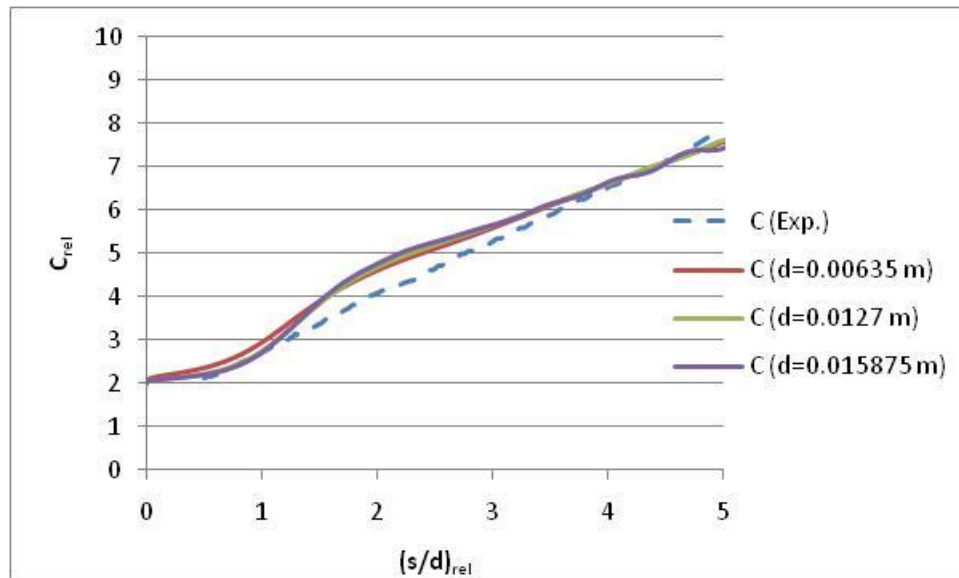
Figure 2.12: Numerical results for different diameters (experimental data from Sarpkaya and Garrison [13]).

The numerical experiment included several different initial velocities, accelerations and cylinder diameters. The results shown in Figure 2.12 show the data correlates fairly well regardless of the cylinder diameter.

The results presented in Figures 2.10- 2.12 show that the values of C versus s/d correlate well regardless of the initial velocity, acceleration or cylinder diameter. These results are also compared to the experimental results of Garrison[14] and Sarpkaya and Garrison[13] for which the relative variables are also applied. Initially the numerical results show that the value of C corresponds to values that would be indicated by potential flow calculations. It should be noted that the experimental results for the initial stages of accelerated motion (s/d<0.5) were estimated in the experiments described in the literature. The numerical results in this region then follow the trend of increasing almost linearly with a constant slope.

2.7 Determining Unsteady Added Mass and Drag Coefficient

Once the force has been calculated it must still be split into the appropriate components of unsteady added mass and drag. This section includes the development of two methods for achieving this goal.

2.7.1 Equation of a Line Method

On further inspection of Equation 2.25, the relationship between the force in the direction of the flow and the unsteady drag and added mass is similar to an equation of a line.   The method presented here is abbreviated to ELM which stands for Equation of a Line Method. The equation of a line can be expressed as,

$$y = mx + b. \tag{2.26}$$

Relating the coefficients in Equation 2.25 to the coefficients in Equation 2.26,

$$m = \frac{4C_D}{\pi} \qquad (2.27)$$

and

$$b = C_M \qquad (2.28)$$

The function for a specific value of s/d can be calculated by fitting a second order Lagrange interpolating polynomial to each set of three adjoining data points. This can then be differentiated analytically to determine the slope, m as expressed in Equation 2.29. This method is ideal for unequally spaced values of s/d.

$$\begin{aligned} m = f'(x) \cong f(x_{i-1}) &\frac{2x - x_i - x_{i+1}}{(x_{i-1} - x_i)(x_{i-1} - x_{i+1})} \\ + f(x_i) &\frac{2x - x_{i-1} - x_{i+1}}{(x_i - x_{i-1})(x_i - x_{i+1})} \\ + f(x_{i+1}) &\frac{2x - x_{i-1} - x_i}{(x_{i+1} - x_{i-1})(x_{i+1} - x_i)}. \end{aligned} \qquad (2.29)$$

Once the slope (m) and intercept (b) of each point is determined, the unsteady drag coefficient and the added mass coefficient can be determined from the following relations,

$$m = \frac{C_{i+1} - C_{i-1}}{\left(\frac{S_{rel}}{d}\right)_{i+1} - \left(\frac{S_{rel}}{d}\right)_{i-1}} = \frac{4}{\pi}C_D \qquad (2.30)$$

and

$$C_M = C - m\frac{S_{rel}}{d} = C - C_D\frac{4}{\pi}\frac{S_{rel}}{d} \qquad (2.31)$$

2.7.2 Application of ELM

The technique of fitting the data to an equation of a line (ELM) described in section 2.6.1 is applied to the experimental data presented by Sarpkaya and Garrison[13].

It is then compared to the added mass and unsteady drag coefficients determined using their vortex technique method as shown in Figure 2.13.
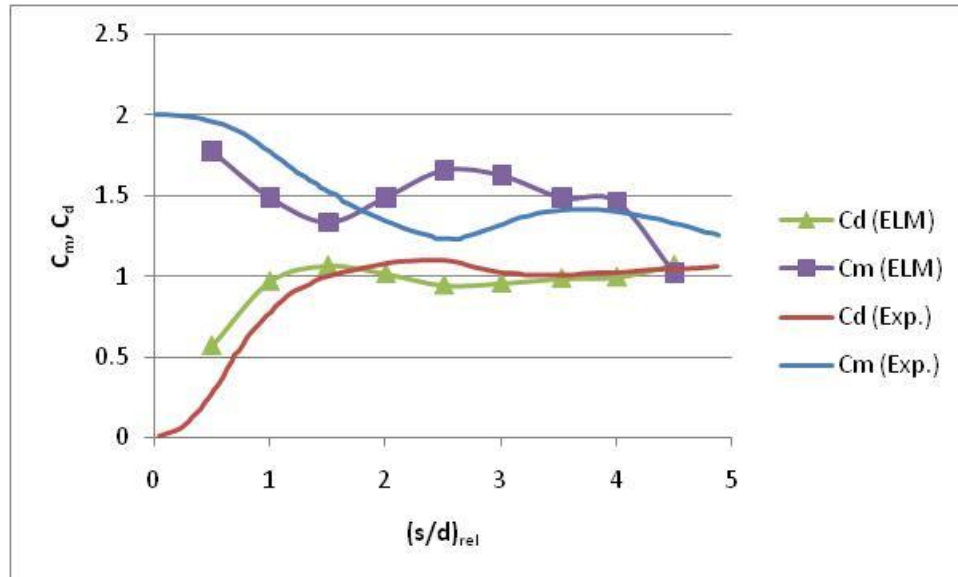
Figure 2.13: Added mass coefficient (purple line) and unsteady drag coefficient (green line) using Equation of a Line Method (ELM) applied to experimental data, compared with results from Sarpkaya and Garrison[13] using vortex technique.

It can be seen that the shape of the curve is similar in both cases although the values are not the same.

2.7.3 Optimized Cubic Spline Method

The unsteady drag and added mass determined by Sarpkaya and Garrison[13] can be expressed in the form of two curves as shown in Figure 2.14, however a simple polynomial fit is not sufficient to accurately fit the data.
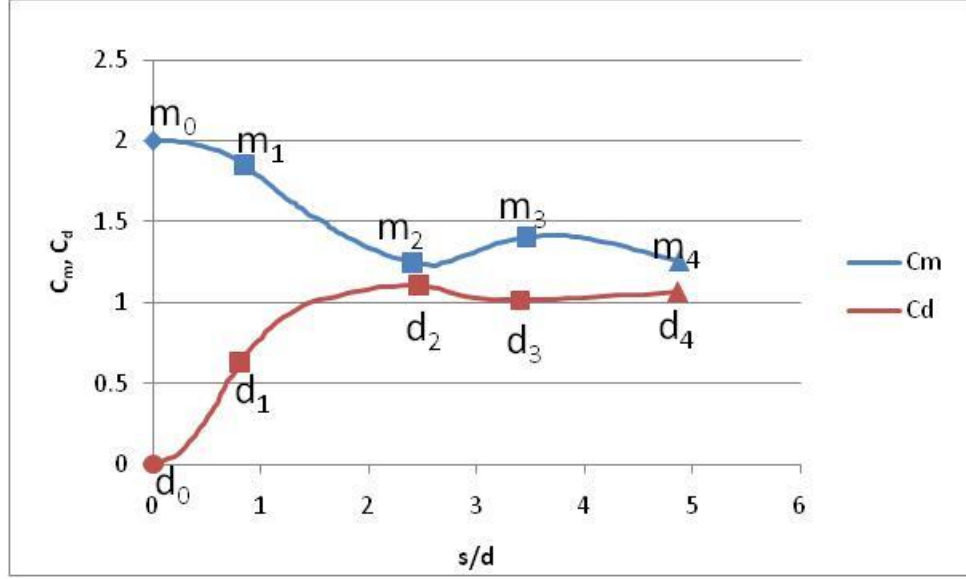
Figure 2.14: Schematic representation of the nodes used in Optimized Cubic Spline Method.

In order to determine the components of the dimensionless force (C) in terms of the added mass coefficient (C_m) and the unsteady drag coefficient (C_d) a cubic spline is used. The method described in this section is called the Optimized Cubic Spline Method and is given the acronym of OCSM. Using cubic splines, two equations are developed similar to those used by Mclain[45]; one for the added mass coefficient and one for the unsteady drag coefficient. The equation for the added mass was developed in terms of the variables m_0-m_4 located at the knot values $(s/d)_{rel,1}$, $(s/d)_{rel,2}$, $(s/d)_{rel,3}$ and $(s/d)_{rel,4}$ while the equation for the unsteady drag was developed in terms of d_0-d_4 also located at the knot values $(s/d)_{rel,1}$, $(s/d)_{rel,2}$, $(s/d)_{rel,3}$ and $(s/d)_{rel,4}$. The knot values for the x axis are the same for both curves. The variable d_0 is restrained in both the s/d and C_d, directions;

$$\left(\frac{s}{d}\right)_{rel,d_0} = 0, \tag{2.32}$$

$$(C_d)_{d_0} = 0. \tag{2.33}$$

The variable m_0 is restrained in the s/d direction but unrestrained in the C_m direction;

$$\left(\frac{s}{d}\right)_{rel,m_0} = 0, \tag{2.34}$$

40

$$(C_m)_{m_0} = m_0. \tag{2.35}$$

The variables m_1-m_4 and d_1-d_4 have no restraints in either the C_m, C_d or the $(s/d)_{rel}$ directions;

$$\left(\frac{s}{d}\right)_{rel,m_1} = x_1, (C_m)_{m_1} = m_1, (C_d)_{d_1} = d_1, \tag{2.36}$$

$$\left(\frac{s}{d}\right)_{rel,m_2} = x_2, (C_m)_{m_2} = m_2, (C_d)_{d_2} = d_2, \tag{2.37}$$

$$\left(\frac{s}{d}\right)_{rel,m_3} = x_3, (C_m)_{m_3} = m_3, (C_d)_{d_3} = d_3, \tag{2.38}$$

$$\left(\frac{s}{d}\right)_{rel,m_4} = x_4, (C_m)_{m_4} = m_4, (C_d)_{d_4} = d_4. \tag{2.39}$$

The cubic equation for each interval can be expressed in the form given by Chapra and Canale[61] as;

$$
\begin{aligned}
f_i(x) = {} & \frac{f''(x_{i-1})}{6(x_i - x_{i-1})}(x_i - x)^3 + \frac{f''(x_i)}{6(x_i - x_{i-1})}(x - x_{i-1})^3 \\
& + \left[\frac{f(x_{i-1})}{x_i - x_{i-1}} - \frac{f''(x_{i-1})(x_i - x_{i-1})}{6}\right](x_i - x) \\
& + \left[\frac{f(x_i)}{x_i - x_{i-1}} - \frac{f''(x_i)(x_i - x_{i-1})}{6}\right](x - x_{i-1}).
\end{aligned}
\tag{2.40}
$$

The second derivatives for the internal knots can be determined using the following equation;

$$
\begin{aligned}
(x_i - x_{i-1})&f''(x_{i-1}) + 2(x_{i+1} - x_{i-1})f''(x_i) \\
& + (x_{i+1} - x_i)f''(x_{i+1}) \\
& = \frac{6}{(x_{i+1} - x_i)}[f(x_{i+1}) - f(x_i)] \\
& + \frac{6}{(x_i - x_{i-1})}[f(x_{i-1}) - f(x_i)].
\end{aligned}
\tag{2.41}
$$

The second derivatives need to be determined first for each of the two curves (added mass and unsteady drag). For the first interval of the added mass equations,

$$x_{i-1} = x_0 = 0, f(x_{i-1}) = f(x_0) = m_0 , f"(x_{i-1})=f"(x_0) = 0, \tag{2.42}$$

$$x_i = x_1 , f(x_i) = f(x_1) = m_1 , f"(x_i)= f"(x_1), \tag{2.43}$$

$$x_{i+1} = x_2, f(x_{i+1}) = f(x_2) = m_2 , f"(x_{i+1})= f"(x_2). \tag{2.44}$$

Therefore Equation 2.41 becomes,

$$(x_1)(0)+2(x_2)f(x_1)+(x_2\text{-}x_1)f(x_2)$$
$$= \frac{6}{(x_2 - x_1)}[m_2 - m_1] + \frac{6}{(x_1)}[m_0 - m_1]. \tag{2.45}$$

Rearranging Equation 2.45 gives,

$$2(x_2)f(x_1)+(x_2 - x_1)f(x_2)$$
$$= m_0 \left[\frac{6}{(x_1)}\right] - m_1 \left[\frac{6}{(x_2 - x_1)} + \frac{6}{(x_1)}\right]$$
$$+ m_2 \left[\frac{6}{(x_2 - x_1)}\right]. \tag{2.46}$$

Similarly, the equations can be developed for the second and third interval giving a system of linear equations with three equations and three unknowns,

$$\begin{bmatrix} 2x_2 & x_2 - x_1 & 0 \\ x_2 - x_1 & 2(x_3 - x_1) & x_3 - x_2 \\ 0 & x_3 - x_2 & 2(x_4 - x_2) \end{bmatrix} \begin{vmatrix} e \\ f \\ g \end{vmatrix}. \tag{2.47}$$

where

$$e = m_0 \left[\frac{6}{(x_1)}\right] - m_1 \left[\frac{6}{(x_2 - x_1)} + \frac{6}{(x_1)}\right] + m_2 \left[\frac{6}{(x_2 - x_1)}\right], \tag{2.48}$$

$$f = m_1 \left[\frac{6}{(x_2 - x_1)}\right] - m_2 \left[\frac{6}{(x_3 - x_2)} + \frac{6}{(x_2 - x_1)}\right]$$
$$+ m_3 \left[\frac{6}{(x_3 - x_2)}\right], \tag{2.49}$$

and

$$g = m_2 \left[\frac{6}{(x_3 - x_2)} \right] - m_3 \left[\frac{6}{(x_4 - x_3)} + \frac{6}{(x_3 - x_2)} \right]$$
$$+ m_4 \left[\frac{6}{(x_4 - x_3)} \right]. \tag{2.50}$$

Applying equation 2.40 to interval one gives,

$$C_m(x_1) = f''(x_1) \left[\frac{x^3}{6x_1} - \frac{x_1 x}{6} \right] + m_0 \left[\frac{x_1 - x}{x_1} \right] + m_1 \left[\frac{x}{x_1} \right]. \tag{2.51}$$

In a similar manner, the equations can be developed for intervals 2, 3 and 4. From the equations developed above, a value of C can be calculated and compared with the measured (experimentally or numerically obtained) value of C. The points of the spline, $(s/d)_{rel,1-4}$, m_{0-4} and d_{1-4}, can then be optimized using the method of least squares using the "Solver" function in Excel 2007 to minimize the quantity;

$$\epsilon = \sum (C_{cal} - C_{meas})^2 \tag{2.52}$$

where ϵ is the error that is minimized.

2.7.4 Application of OCSM

The OCSM is applied to the experimental data of Sarpkaya and Garrison[13] and compared to the results of their vortex technique.
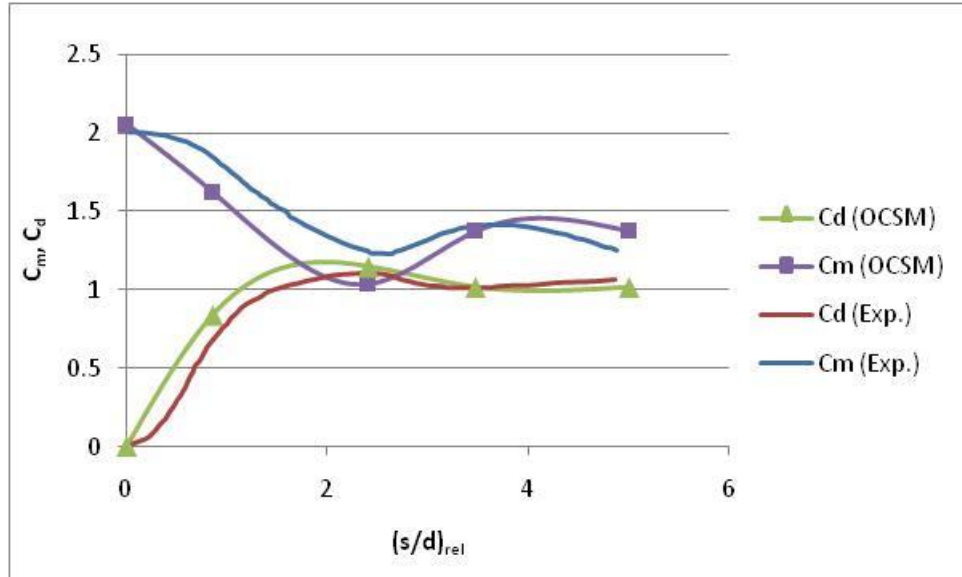
Figure 2.15: Added mass coefficient (purple line) and unsteady drag coefficient (green line) using Optimized Cubic Spline Method (OCSM) applied to experimental data compared with results from Sarpkaya and Garrison[13] using vortex technique (square markers represent the knots).

The comparison is presented in Figure 2.15. The trends are very similar and the values reasonably close to those of the vortex technique.

2.7.5 Discussion of ELM and OCSM

Both techniques produce similar trends to those presented by Sarpkaya and Garrison[13]. The OCSM, however, shows a closer prediction of the actual values than the ELM.

The advantages of the ELM lie in the quick and easy execution of the technique to determine the components of added mass and unsteady drag when given the force measurements (in the form of the dimensionless force C). Since this uses the derivative (slope) of the original data, any noise present in the data is amplified. In order to alleviate this problem the number of data points used for the technique was reduced by taking values every 0.5 s/d. Using the ELM technique the initial value of the added mass coefficient is very close to 2, which is the theoretical value calculated using potential flow. This matches what has previously been accepted as the value for the initial portion of the accelerated flow. The initial value of the unsteady drag coefficient appears to go to approximately zero. It is difficult to determine the exact initial value due to the fact that

experimental data very close to s/d = 0 is not available. Although the general shape of the curve is similar to the experimental results, it is rather severely out of phase with the experimental results (i.e. ELM reaches a maximum while the experimental data is at a minimum).

The advantage of the OCSM is that it yields values closer to those found in the literature. There are no restraints on the initial values of the added mass or on the position of the x value of the spline. It was specified, however, that the knot values must be at least 0.5 s/d apart. It was also specified that the last knot be within the range of the data (s/d<5). This is less restricted than the method used by McLain[45] who had set values for the x (s/d) positions of his spline. Although the unsteady drag coefficient was set to zero for the initial value of the $(s/d)_{rel}$ the added mass coefficient was not constrained for the initial value of s/d (also an improvement over McLain[45]). This resulted in a value that was only 2.71% higher than the theoretical value calculated from potential flow. The disadvantages of this technique are in the application: it is difficult to set up the equations to perform the optimization and it is also very sensitive to the initial (s/d) values used in the optimization process. The optimization process produces a minimum value for the square of the difference between the calculated values of C and the measured value of C. Since the initial guesses produce different results, a measure of how well the curve is optimized can be done by comparing the square of the difference value for each set of initial guesses. The minimum value of the square of the difference is considered the optimal set and is used for the final results. A sequential systematic method was used to determine the best initial guesses.

2.7.6 Application to Fluent Data

Both techniques, ELM and OCSM, have been applied to the experimental data of Sarpkaya and Garrison[13] in order to compare the validity of each of the results. As stated in the previous section ELM is simpler and gives the appropriate shape of the curve, however the maximums and minimums for the ELM do not coincide with the maximums and minimum of the experimental work. The use of OCSM, may be more

complicated to implement, however it gives much better results when compared to the experimental data. Therefore the OCSM will be applied for any further data processing.

The OCSM is applied to the results of the numerical experiments and presented in Figure 2.16. Due to the differences between the numerical and experimental values of C versus s/d, it is not expected that the resulting curves be the same. The experimental curves are included simply to illustrate the differences.
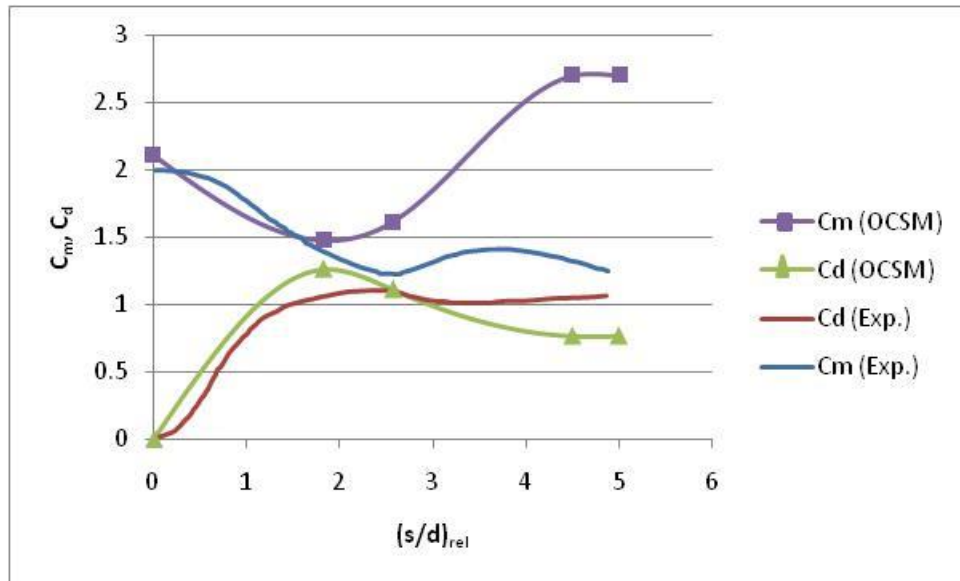
Figure 2.16: Added mass coefficient (purple line) and unsteady drag coefficient (green line) using Optimized Cubic Spline Method (OCSM) applied to numerical data, compared with results from Sarpkaya and Garrison[13] using vortex technique (square markers represent the knots).

From Figure 2.16 it can be seen that there are some differences in the application of OCSM to the numerical results when compared with the experimental results. As discussed in Section 2.6.3 the initial value of C_m is not restrained. The results show that the initial value of C_m calculated by the OCSM is 2.11. This is 5.57% higher than the theoretically calculated value of 2, which is what is expected for the initial portion of acceleration. From Figure 2.16 it is also apparent that the unsteady drag is larger in the range of $(s/d)_{rel}$ from 1 to approximately 2. This corresponds to the "hump" that was discussed in Section 2.5.5. The difference in the slope of the dimensionless force curve is amplified by the separation into unsteady drag and added mass coefficients manifesting itself as a larger value of the added mass coefficient and a relatively smaller value of the unsteady drag for s/d ranges above 3.

46

Chapter 3 - Experimental Study of Added Mass of a Sphere Falling from Rest in a Stationary Fluid

This chapter begins with the development of the dimensionless force for a sphere, similar in form to that developed for the cylinder, assuming a constant acceleration over the range of motion of the experimental data. This is followed by a detailed description of the method used in the experiments. The basic methodology behind the experiments is to use a high speed, high resolution camera to record the position of the sphere as it falls.

Then the procedure used to analyze the images in order to calculate the position and corresponding time is presented. From the time and displacement of the sphere the acceleration is then calculated. The acceleration is then used along with Newton's Second law in order to determine the forces acting on a sphere, one of which is the force due to added mass. The results are presented in a dimensionless form similar to those of the cylinder.

Finally, two methods are applied to the dimensionless forces in order to indirectly determine the added mass. The first method uses the assumption of no drag forces, while the second method includes the drag and a modified version of that used in the cylinder analysis.

3.1 Dimensionless Force Formulation for a Sphere

Similar to the equations for the cylinder, the dimensionless force for the sphere can be developed as indicated below. The equations are an application of Newton's second law to the sphere shown in Figure 3.1,
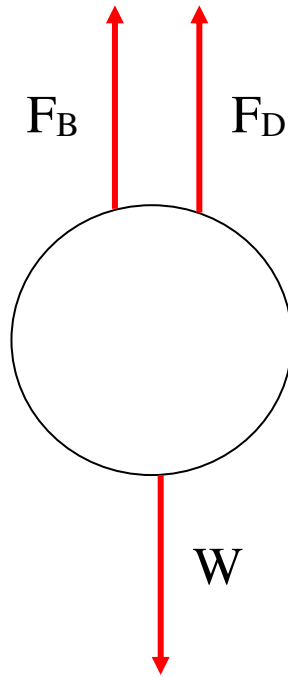
Figure 3.1: Diagram of forces acting on a sphere.

This results in,

$$(M + M_{add})a = W - F_B - F_D, \tag{3.1}$$

where M is the mass of the object, M_{add} is the added mass of the object, a is the acceleration, W is the weight of the object, F_B is the buoyant force and F_D is the drag force. The drag force can be expressed as follows,

$$F_D = C_D \frac{1}{2}\rho V^2 A, \tag{3.2}$$

where

$$A = \frac{\pi d^2}{4}. \tag{3.3}$$

Substituting Equations 3.2 and 3.3 into Equation 3.1 and rearranging yields,

$$(M + M_{add})a + C_D \frac{1}{2}\rho V^2 \frac{\pi d^2}{4} = W - F_B. \tag{3.4}$$

It should be noted that the acceleration for the cylinder is held constant. In this set of experiments constant acceleration is only an approximation. This approximation is more accurate closer to the beginning of acceleration where the drag forces are zero. One of the assumptions for the range of data of interest is that the drag is very small but not zero.

In order to obtain equations in terms of s/d the following relations are needed,

$$s = \frac{at^2}{2}, \tag{3.5}$$

and

$$V = \frac{s}{t}. \tag{3.6}$$

Rearranging Equation 3.5 gives,

$$a = \frac{2s}{t^2}. \tag{3.7}$$

The theoretical added mass can be expressed as,

$$M_{add.the} = \frac{\rho \pi d^3}{12}. \tag{3.8}$$

Dividing Equation 3.4 by the force associated with the added mass (Equation 3.8 multiplied by acceleration) results in,

$$\frac{(M + M_{add})}{M_{add,the}} + \frac{\frac{C_D}{2}\rho \frac{V^2 \pi d^2}{4}}{M_{add,the} a} = \frac{W - F_B}{M_{add,the} a}. \tag{3.9}$$

This can also be expressed as

$$\frac{(M + M_{add})}{\frac{\rho \pi d^3}{12}} + \frac{\frac{C_D}{2}\rho \frac{V^2 \pi d^2}{4}}{\frac{\rho \pi d^3}{12} a} = \frac{W - F_B}{\frac{\rho \pi d^3}{12} a}. \tag{3.10}$$

49

Simplifying Equation 3.10 gives

$$\frac{(M + M_{add})}{\frac{\rho \pi d^3}{12}} + \frac{3}{2} C_D \frac{V^2}{da} = \frac{W - F_B}{\frac{\rho \pi d^3}{12} a}. \tag{3.11}$$

Substituting Equation 3.6 and 3.7 into Equation 3.11 gives,

$$\frac{(M + M_{add})}{\frac{\rho \pi d^3}{12}} + \frac{3}{2} C_D \frac{\left(\frac{s}{t}\right)^2}{d\left(\frac{2s}{t^2}\right)} = \frac{W - F_B}{\frac{\rho \pi d^3}{12} a}. \tag{3.12}$$

Simplifying Equation 3.12 gives,

$$\frac{(M + M_{add})}{M_{add,the}} + \frac{3}{4} C_D \frac{s}{d} = \frac{W - F_B}{M_{add,the} a}. \tag{3.13}$$

The added mass coefficient is the ratio of the added mass to the theoretical added mass,

$$C_M = \frac{M_{add}}{M_{add,the}}. \tag{3.14}$$

Substituting Equation 3.14 into Equation 3.13 gives,

$$\frac{(M)}{M_{add,the}} + C_M + \frac{3}{4} C_D \frac{s}{d} = \frac{W - F_B}{M_{add,the} a}. \tag{3.15}$$

Rearranging Equation 3.15 gives,

$$\left[\frac{W - F_B}{a} - M\right] \frac{1}{M_{add,the}} = C_M + \frac{3}{2} C_D \frac{s}{d} = C. \tag{3.16}$$

This is very similar in form to the dimensionless force variable developed for the cylinder and is used in analyzing the experimental data obtained from the experiments described below.

3.2 Experimental Equipment

This section describes the equipment used in order to perform the experiments on the falling sphere.
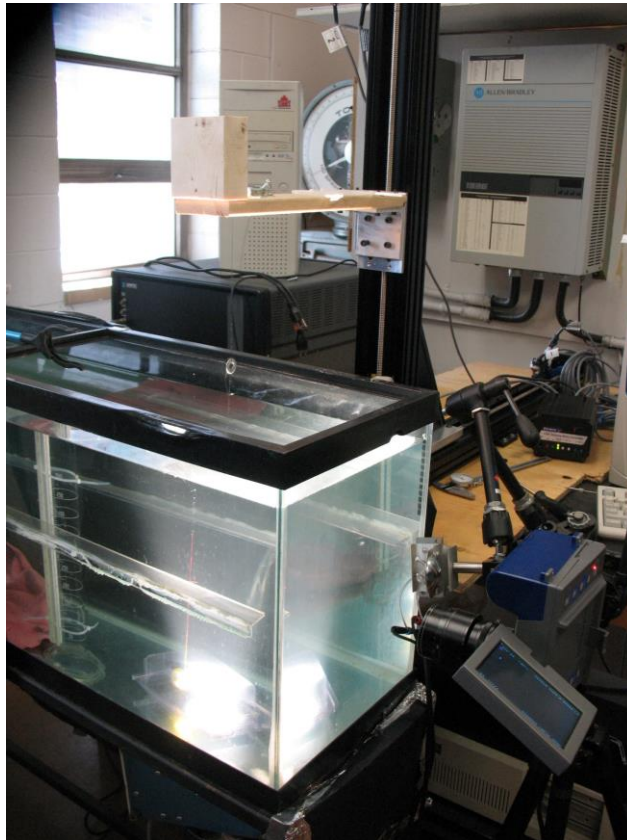
Figure 3.2: Picture of experimental equipment for spheres falling from rest.
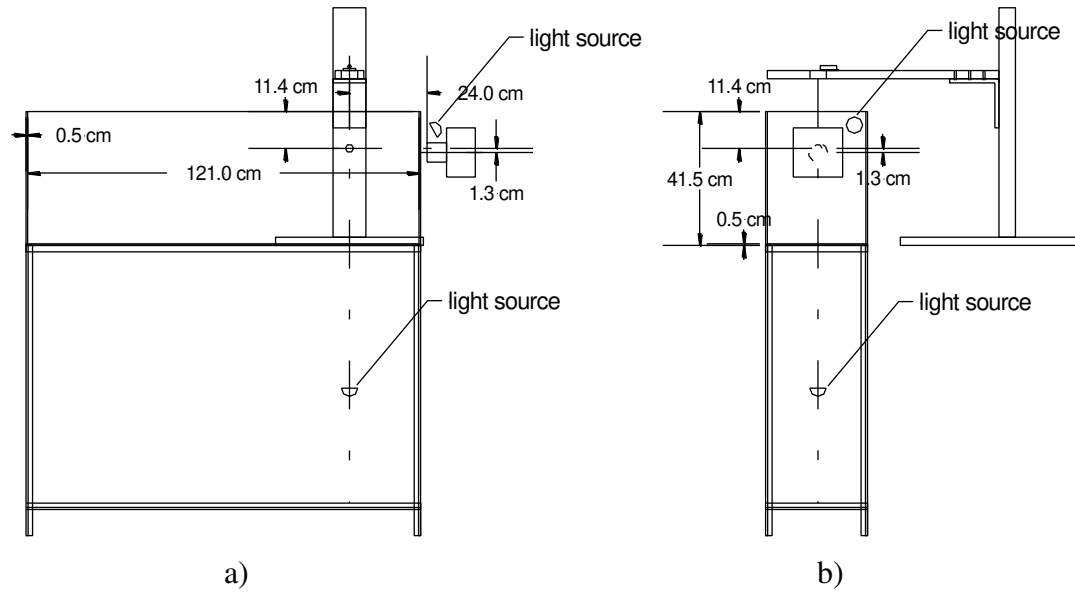
Figure 3.3: Schematic of experimental set up a) side view, b) front view.

The experimental set up is shown in Figure 3.2 with a schematic shown in Figure 3.3. It consists of a tank, a sphere, a sphere release mechanism, a high speed camera, two light sources and a traverse. The tank has the dimensions of 38 cm deep, 30 cm wide and 120 cm long. The properties of the spheres can be seen in Table 3.1.

Sphere No.	Material	Diameter (m)	Mass (kg)	Weight-Buoyant Force (N)	Avg Acceleration (m/s^2)
1	Stainless Steel (hollow)	0.0254	0.01912	0.1036	4.00
2	Stainless Steel (hollow)	0.0254	0.01937	0.1059	4.08
3	Brass	0.01905	0.03065	0.2642	7.98
4	Brass	0.01905	0.03066	0.2641	7.98
5	Stainless Steel (solid)	0.0254	0.06702	0.5716	7.90
6	Stainless Steel (solid)	0.0254	0.06704	0.5742	7.95

Table 3.1: Properties of the spheres.

The material and diameter of the spheres are determined from manufacturer specifications. The mass of the sphere is determined using a scale with a ±0.0005 g uncertainty. The weight minus the buoyant force is determined by weighing the sphere suspended in water at room temperature. The water that is not allowed to touch the scale therefore the scale measures the net force downward, which is the weight of the object acting in a downward direction minus the buoyant forces of the water acting in the upward direction. The determination of the acceleration will be developed in later sections.

The spheres were painted yellow in order to yield a better image using the high speed camera. Care was taken to ensure that the finish is smooth and even. A thread was attached to the spheres using a small amount of high strength adhesive. Several different types of thread material were tested and the easiest to work with was found to be cotton thread. The amount and form of the adhesive was deemed to be negligible to overall symmetry of the sphere. The effect of the string (drag and added mass) was determined to be a negligible portion of the overall forces.
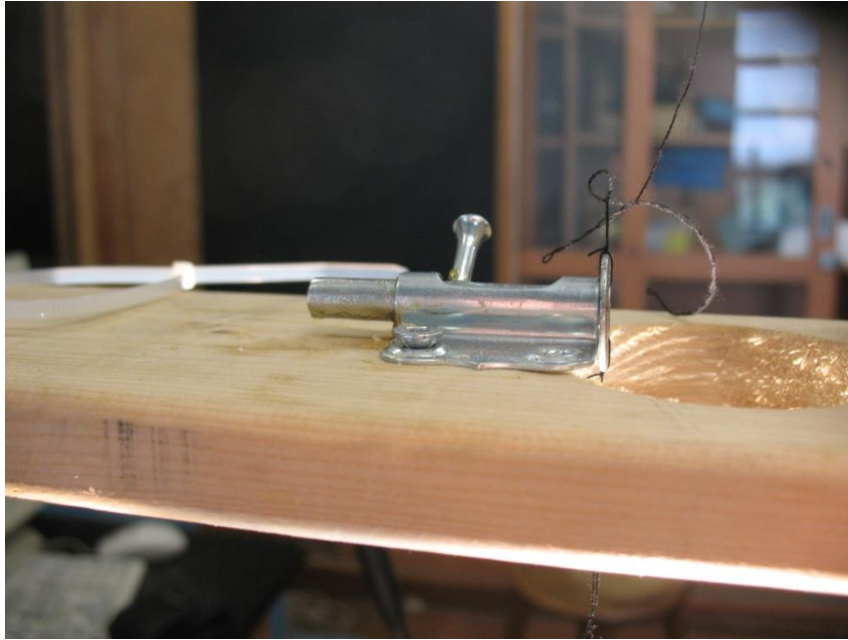
Figure 3.4: Release mechanism for falling sphere.

Preliminary experimentation utilizing a manual release of the string revealed that the release conditions such as initial zero velocity, could not accurately be established. Several different release mechanisms were attempted in order to overcome this problem. These included various forms of friction release as well as burning the thread. A high speed camera was used to determine the repeatability of the release mechanism. The best results are obtained with the simple device shown in Figure 3.4. This consists of attaching the thread to the sphere and the other end of the thread to a washer. The washer is then balanced on the rod and set flush to the housing of the sliding rod mechanism. The rod is quickly moved, which in turn releases the washer and the sphere. The washer is not allowed to disturb the water by installing a device which catches it before it hits the water surface.
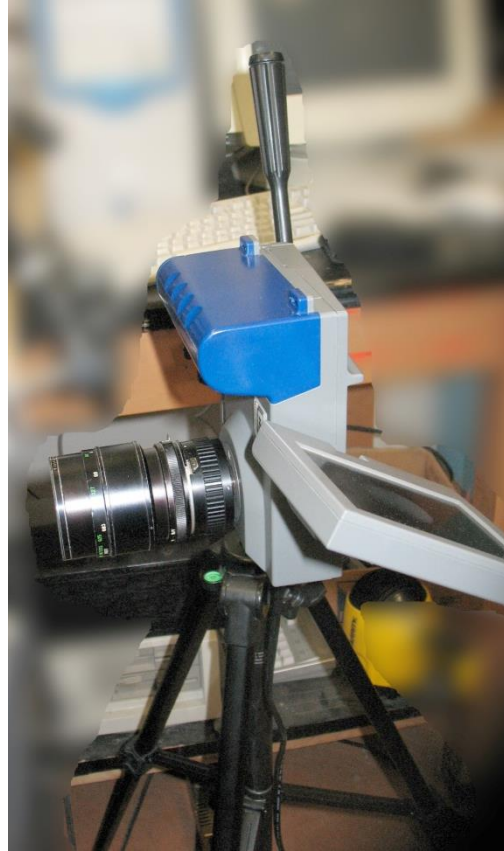
Figure 3.5: Picture of Fastec high speed camera.

A Fastec Trouble Shooter high speed camera as shown in Figure 3.5 is used to record the descent of the spheres. The Fastec camera is capable of capture speeds of 1000 fps and has an image resolution of 1280 x 512 pixels. The resulting video files are in the .avi format which makes it easy to transfer the files to a computer for post processing. A Vivitar 55 mm Auto Macro camera lens is used on the camera which is meant to help reduce parallax effects.

Two high intensity incandescent light sources are required in order to illuminate the sphere sufficiently to be captured by the high speed camera. The spheres are lit from below and in front of the tank. It is important that the bottom of the sphere be properly lit to produce a clean image for post processing. The back and the sides of the tank are blacked out in order to aid in the production of a higher contrast image of the sphere.

The traverse is used in order to ensure the accurate positioning of the sphere relative to the camera at the onset of each set of runs. The distance that the traverse can be programmed to move is accurate to within 0.001 inches. This allows an accurate

calibration of the position of the sphere on the photos to a real distance measurement. For example, the sphere is positioned so that just the very bottom of the sphere is in the field of view of the camera then a picture is taken. The traverse then moves the sphere 0.02 m and another picture is taken. Using the bottom of the sphere as a common reference point, the distance the sphere has moved between the two pictures can be measured in pixels. A relationship can then be calculated for the distance, in meters, for one pixel.

3.3 Experimental Procedure

The following section outlines the procedure used in collecting the data for the sphere falling from rest experiment. The calibration procedure is explained first, followed by an explanation of the procedure used to obtain the falling sphere data.

3.3.1 Calibration

The camera is placed next to the tank as close to the sphere as physically possible. This allows for the best possible resolution of the initial stages of the sphere's position. This results in a field of view of approximately 0.0381 m (1.5 inches) in the direction of sphere motion. The lens used on the camera is specifically chosen to reduce the parallax effect of close-up shots. In order to completely eliminate any such effects a simple calibration is performed. Before each set of experiments the camera and sphere are positioned such that only the bottom of the sphere is visible in the camera view. The traverse is then used to lower the sphere a known distance and a picture is taken using the high speed camera. This process is repeated three more times. The result is five pictures equally spaced over the field of view of the camera. The distances are then compared with the number of pixels for each of the corresponding pictures which are then used to calculate the distance per pixel. The distance per pixel is the same throughout the field of view which verifies that there is no parallax effect. This calibration also accounts for any possible refraction since it relates a physical measurement to the pixels for the corresponding movement of the sphere. The distance between subsequent pictures (five

different pictures over a 0.0381 m field of view) is sufficiently small to account for any possible refraction over the entire field of view. Pictures are taken of the initial position and the final position in which the bottom of the sphere is as close as possible to the bottom of the field of view of the camera. The other intermediate pictures produce the same distance/ pixel ratio so only two images are needed. The known distance between the two images are compared with the number of pixels between the bottom-most point on the sphere. This distance/pixel measurement is used in calculating the distance moved by the sphere for the experiments.

The thread used to suspend the sphere in place is illuminated and a high resolution picture is taken. This image is then be used to account for any deviation from the vertical in the image.

3.3.2 Experiments

The experiments consisted of a sphere falling from rest in an otherwise stationary fluid. Three different accelerations, accomplished by using spheres of different weight, are examined. The specifics of the sphere properties can be seen in Table 3.1. The following steps are followed in acquiring one set of images.

1) The sphere is suspended by a string at least 4.5 diameters[7] below the surface of the water.

2) The sphere is allowed to come to rest.

3) The lighting from the bottom and front of the tank are adjusted to produce maximum illumination of the sphere.

4) The camera is placed on a tripod and leveled in order to get an image that is parallel to the string in the vertical plane and parallel to the bottom of the tank in the horizontal plane.

5) The camera is then "zoomed in" until the bottom of the sphere is visible at the top of the frame and 1.5 inches of the test section are visible.

6) The string is illuminated and a high resolution picture is taken in order to adjust for any discrepancies in the angle of the camera (the photos are rotated if the camera is found to be skewed).

7) The camera is triggered and the sphere is released. It is not necessary that the timing of the sphere's release and the triggering of the camera be synchronized. Any synchronization problems between the start of the filming and the start of the sphere's decent are accounted for in the image processing.

This procedure gives the results for a single run of a single sphere, however, the experiment consists of 30 runs for each sphere. In a few cases it was obvious that something had interfered with the experiment and hence the data were not realistic and were discarded. This results in 30 runs for sphere 1, 28 runs for sphere 2, 29 runs for sphere 3, 28 runs for sphere 4, 27 runs for sphere 5 and 25 runs for sphere 6. Looking at Table 3.1, for which the properties of each of the six spheres is presented, the spheres are separated into three different groups. Each group consists of two spheres of similar properties (mass, diameter and acceleration) in order to demonstrate repeatability for a given set of properties. Spheres 1 and 2 are grouped together, similarly spheres 3 and 4 as well as 5 and 6. Each group includes the data from both spheres for that grouping and is presented using a non-dimensional diameter as well as a non-dimensional acceleration. The non-dimensional diameter is the diameter of the sphere divided by the diameter of the largest sphere d_0, where $d_0 = 0.0254$ m. The non-dimensional acceleration is the average acceleration, as described in Section 3.4.1, of all viable runs divided by gravitational acceleration g, where g = 9.81 m/s^2.

3.4 Image Processing Procedure

Each experimental run is capture using the Fastec Trouble Shooter camera with a capture speed of 1000 fps and a resolution of 1280 x 512 pixels. The .avi files are then transferred to a PC where Photran Fastcam Viewer 3 is used to convert each individual frame of the avi file into a .jpg picture file. Example images are shown in Figure 3.6.

a   b   c
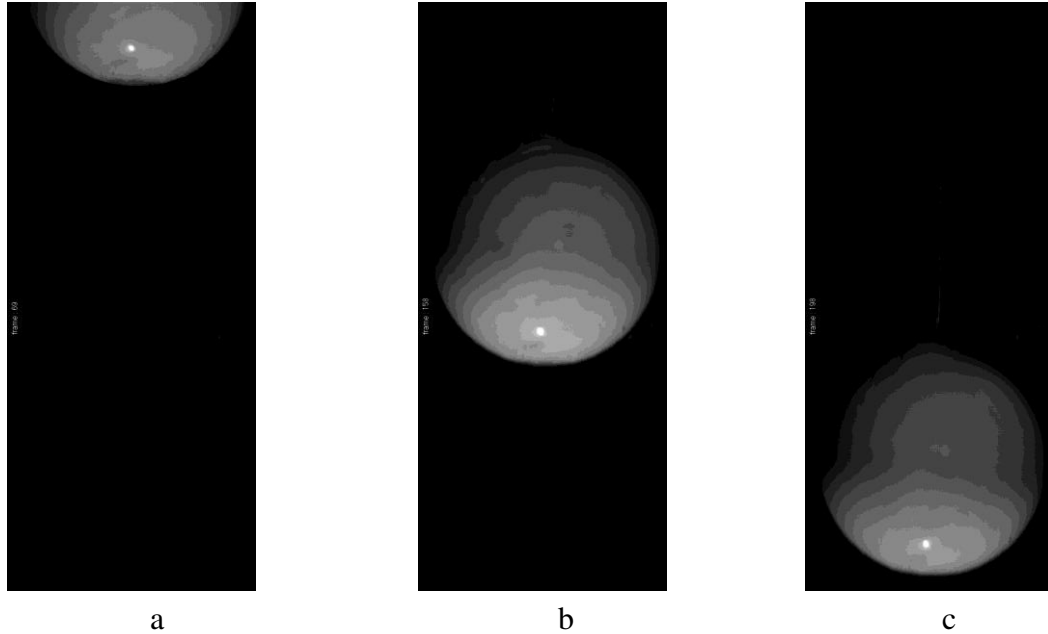
Figure 3.6: Pictures from .avi file. a) beginning of run, b)midway through run, c)end of run

The images are then processed using the photo editing software Photoshop CS5 Professional Extended. The images are cropped and converted to black and white photos using Photoshop's threshold function as shown in Figure 3.7.   The distance is measured from the bottom of the sphere to the bottom of the field of view for each image.
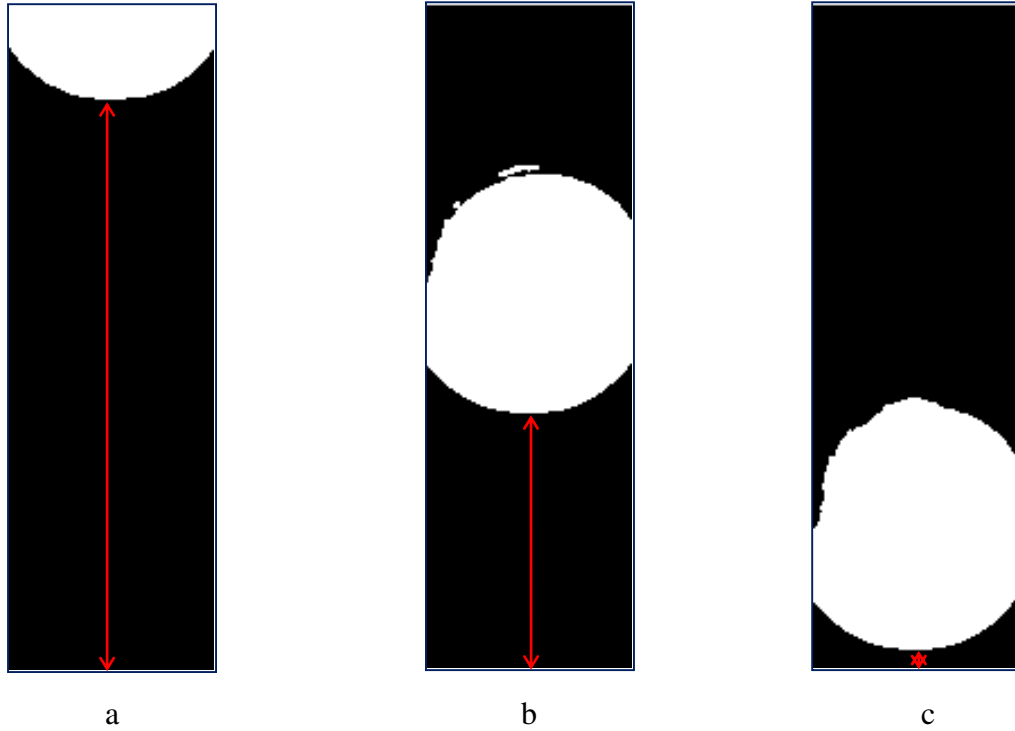
Figure 3.7: Images cropped and transformed using threshold function. The red arrows indicate the measurements taken. a)beginning of run, b) midway through run, c)end of run.

The distance is measured in pixels, for the first picture, then subtracted from subsequent measurements in order to get the distance as it changes with time.

$$s_i = Measurement_i - Measurement_1. \tag{3.17}$$

The time for each measurement is determined using the prescribed camera speed,

$$t_i = \frac{1}{1000 \, fps} \times frame\#. \tag{3.18}$$

The result is a set of displacements with respect to time.

3.4.1 Acceleration Calculations

Using a finite difference approach to estimate the acceleration of the sphere was initially attempted, but resulted in extremely noisy results. Therefore, an alternative

method is needed that allowed for smoothing of the data. The final result is a method for calculating the acceleration that grouped the data in sets of 70 with overlapping data points as indicated in Figure 3.8. The data set consisting of 70 points was found to be the lowest value of data points with an acceptable level of noise reduction. Data points 1-70 are used to determine the velocity and acceleration that corresponded to the time for point 35. The data set is then moved by one data point (i.e. points 2-71 determine velocity and acceleration for time corresponding to point 36). This gives a moving calculation for the acceleration and velocity.

Time (t)	Displacement (S)			2nd Order Coefficient (x 2)
1	S1			
2	S2			
3	S3			
.	.			
.	.			
35	S35			Acc 35
36	S36			Acc 36
37	S37			Acc 37
.	.			
.	.			
70	S70			
71	S71			
72	S72			

Figure 3.8: Acceleration calculations.

Each set of data is fitted with a second order polynomial curve using the LINEST function in an Excel spreadsheet. The second order coefficient is used to determine the acceleration. The curve fitting algorithm in Excel will result in the first and second order coefficients as well as the y intercept which has the following form

$$y = a_2 x^2 + a_1 x + a_0,$$
(3.19)

61

where $y = distance = s$ and $x = time = t$. Rewriting Equation 3.19 in terms of distance and time;

$$s = a_2 t^2 + a_1 t + a_0. \tag{3.20}$$

This is similar, in form, to the equation of motion for a particle

$$s = \frac{1}{2} a t^2 + V_o t + s_o, \tag{3.21}$$

where a = acceleration, V_o = initial velocity and s_o = initial position.

Equation 3.21 assumes that the acceleration is constant. For the range of each curve fit (70 data points) this is an acceptable assumption. The second order coefficient can be related to the acceleration,

$$a = 2a_2. \tag{3.22}$$

This is the acceleration calculated for the distance corresponding to 35th (midpoint of the data range) point.

The following graphs show the experimentally determined acceleration with respect to s/d for the cases considered.
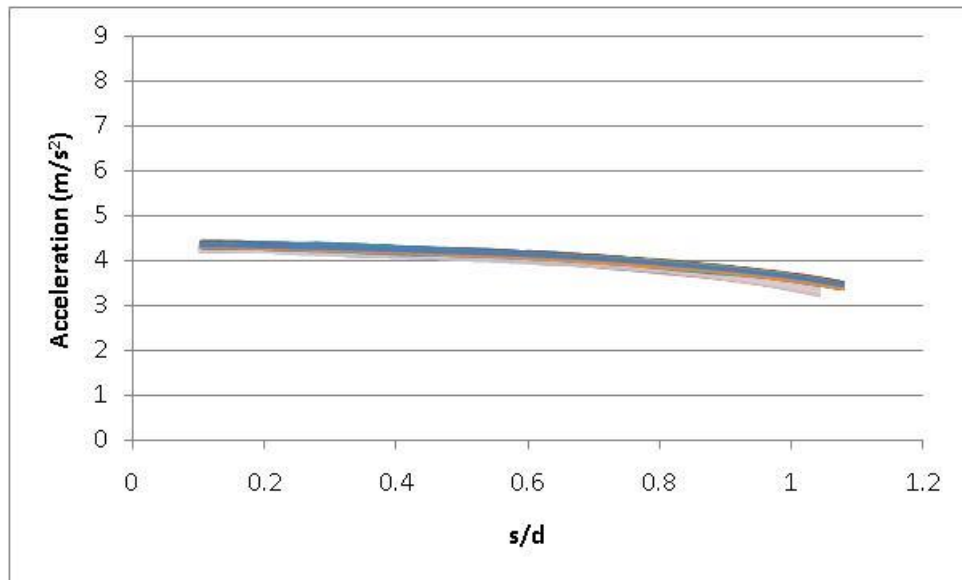
Figure 3.9: Acceleration curves for 58 runs for d/d$_o$ = 1, a/g=0.43 (d$_o$=0.0254 m, g=9.81 m/s^2).
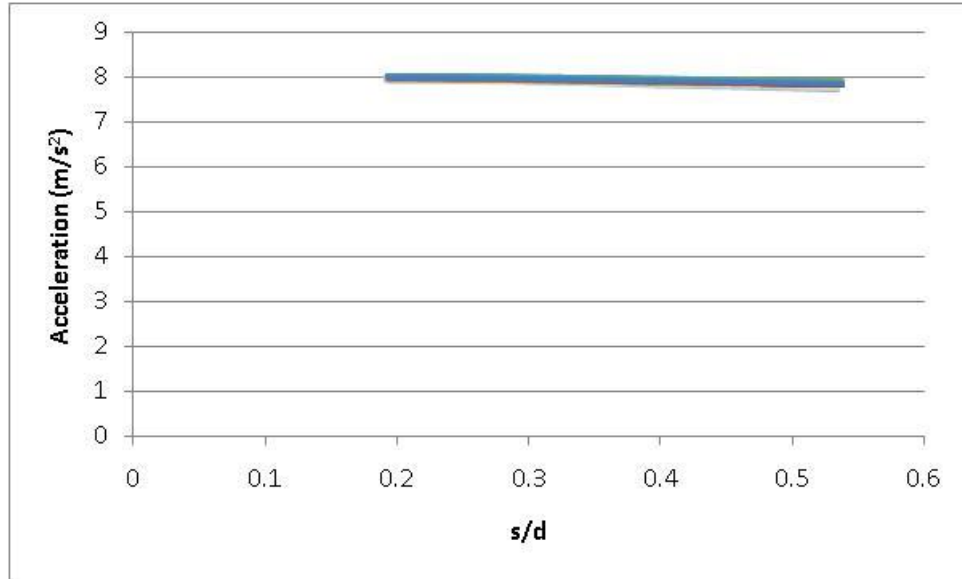
Figure 3.10: Acceleration curves for 52 runs for $d/d_o = 0.75$, $a/g = 0.82$ (d_o=0.0254 m, g=9.81 m/s^2).
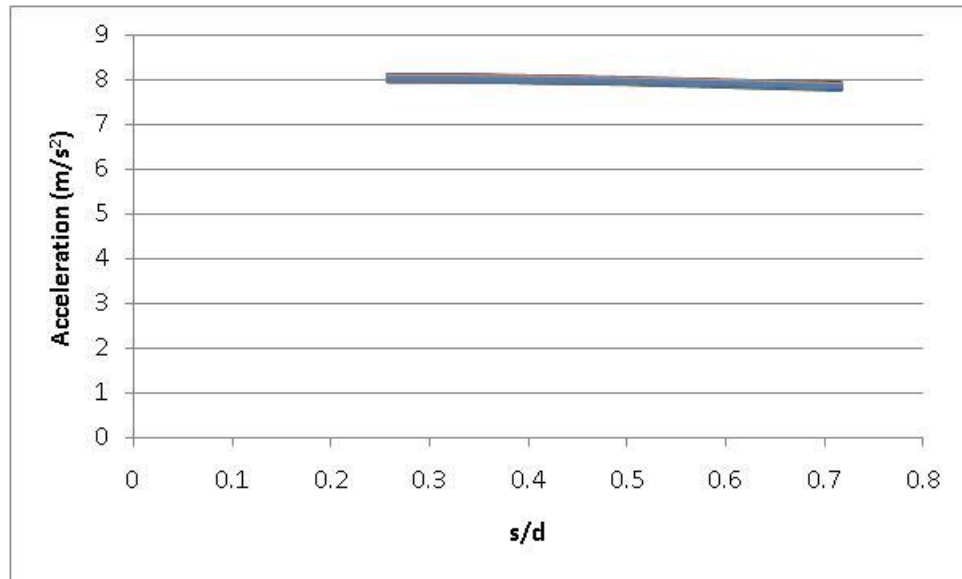
Figure 3.11: Acceleration curves for 57 runs for $d/d_o = 1$, $a/g = 0.82$(d_o=0.0254 m, g=9.81 m/s^2).

Figure 3.9 shows the acceleration calculated for the 58 runs performed for spheres 1 and 2 as described in Table 3.1.(each curve represents the acceleration of a different run). The acceleration changes by approximately 22% from its original value for the range of data collected for $d/d_o = 1$, a/g=0.43; however, if the data are limited to a range

that is common for all three groups of spheres ($0.1 < s/d < 0.8$) the acceleration only changes by approximately 7.2%. Therefore the data for this sphere will be limited for the remainder of the analysis.

Figure 3.10 shows the acceleration curves calculated for the 52 runs performed for spheres 3 and 4 as described in Table 3.1 which are labeled $d/d_o = 0.75$, $a/g = 0.82$ (each curve represents the acceleration calculations for one run). Figure 3.11 shows the acceleration curves for the 57 runs performed for spheres 5 and 6 as described in Table 3.1 which are labeled $d/d_o = 1$, $a/g = 0.82$ (each curve represents the acceleration calculations for one run). The acceleration only changes from the original value by less than 2.5% for both sets of data.

Although one set of data has an acceleration that changes by more than 7%, it is still reasonable to apply the assumption of constant acceleration (even more so for the two data sets that change less than 2.5%).

3.5 Results and Discussion for Sphere

Equation 3.16, developed in Section 3.1, is used to determine the dimensionless force (C) for each set of spheres. All the variables used in Equation 3.16 to calculate the dimensionless force are determined. This includes the Mass of the sphere (M), the Weight of the sphere minus the buoyancy force exerted by the object (W-F_B) (as described in Section 3.2), the theoretical added mass and the acceleration. The dimensionless force (C) is then represented with respect to the dimensionless distance (s/d). The dimensionless distance is calculated using the distance, calculated from Equation 3.5, divided by the diameter of the sphere (d) (see Table3.1). The acceleration required in Equation 3.5 is the average acceleration for all runs at a given time (t).
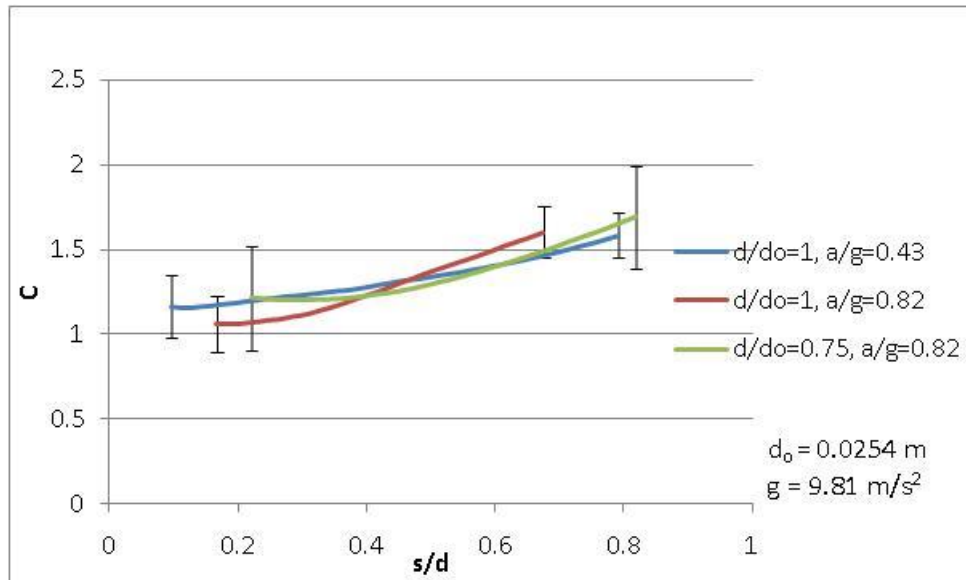
Figure 3.12: C curves for three different sets of spheres with error bars representing the uncertainty.

Figure 3.12 shows the results of each set of spheres using the dimensionless force (C) versus the dimensionless distance, s/d. The results consist of three sets of spheres which contain two different diameters and two different accelerations (see Table 3.1).

Also included in Figure 3.12 are the error bars due to the uncertainty in the measurements. The uncertainties for the measured values of C are approximately 26% for the initial values and approximately 19% at the upper portion of the measurements. The uncertainties in the final measurements stem from the necessity to obtain a second derivative (acceleration) from the experimental data (displacement). The second derivative amplifies any noise in the measurements to such a degree that a smoothing method is necessary to overcome this problem. Although the curve fitting method produces a high uncertainty, the alternative of simply taking the numerical second order derivative had an even higher level of uncertainty. These values (both initial and upper region) are indicated for each of the three curves. A full development of the uncertainty is presented in Appendix B.

From the diagram, the trend of the curves is similar in shape to those presented for the cylinder; the curve is fairly flat during the initial acceleration then increases in a non-linear manner. Although the curve for the $d/d_o = 1$, a/g=0.43 (blue line from Figure 3.12) agrees very well with the curve for $d/d_o = 0.75$, a/g = 0.82 (green line from Figure

65

3.12), there is a difference between those two curves and the one for the $d/d_o = 1$, $a/g = 0.82$ (red line from Figure 3.12). The maximum difference in the curves is 9.7% which is well within the uncertainty of the measurement.

From Chapter 2 it is known that the initial value of the added mass is the theoretical value calculated using potential flow. A sphere accelerating through a stationary fluid has a theoretical added mass coefficient of 1.

Sphere	Initial Value of C	% Difference from Theoretical	Uncertainty (%)
$d/d_o = 1$, $a/g = 0.43$	1.16	15.8	15.8
$d/d_o = 1$, $a/g = 0.82$	1.06	5.95	15.9
$d/d_o = 0.75$, $a/g = 0.82$	1.21	21.4	25.4

Table 3.2: Initial values of C.

Table 3.2 shows the initial values of C and the difference from the theoretical value. The largest difference is that of $d/d_o = 0.75$, $a/g = 0.82$ with a difference of 21.4%. From Figure 3.12 it can be seen that the curve for $d/d_o = 0.75$, $a/g = 0.82$ (green line from Figure 3.12) has a shorter range than the similar curve for $d/d_o = 1$, $a/g = 0.43$ (blue line from Figure 3.12). The value of C for $d/d_o = 1$, $a/g = 0.43$ (blue line from Figure 3.12) at an equivalent s/d would result in a difference from the theoretical value of 19.9%.

3.6 Determining Added Mass and Unsteady Drag for a Sphere

In a similar manner as in the case of the cylinder, the dimensionless force (C) can be separated into the added mass and unsteady drag coefficients.

3.6.1 Assume No Drag

The simplest method of determining the added mass of the sphere is to neglect the drag force. With this assumption Equation 3.23 becomes.

$$\left[\frac{W - F_B}{a} - M\right]\frac{1}{M_{add,the}} = C_M = C \qquad (3.23)$$

However, this assumption is limited to the initial portion of the acceleration.
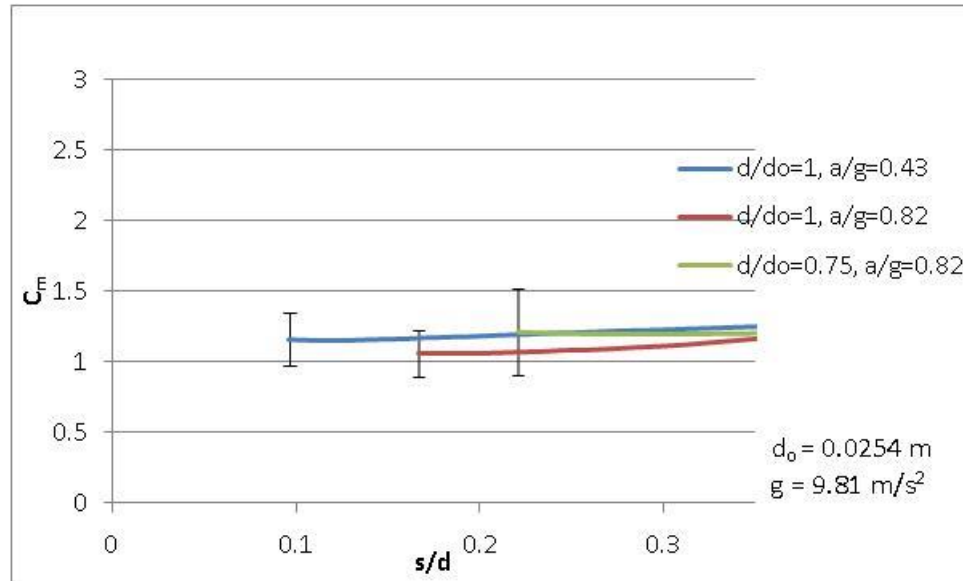
Figure 3.13: Added mass with the assumption of no drag.

The range of applicability for the no drag assumption is chosen such that the values are within 10% of the initial value of C. Using this criteria the range of applicability is $0.1 < s/d < 0.35$ and the resulting values are plotted versus dimensionless distance in Figure 3.13. The uncertainty of the added mass coefficient is the same as that calculated for the dimensionless force in section 3.4. It should be noted that for $d/d_o = 1$, a/g=0.43 and for this range of data, the acceleration does not change more that 2% from the initial value. The other two sets change less than 0.6%. This indicates that the assumption of constant acceleration is even more applicable in this limited range than for the whole range of collected data.

3.6.2 Application of the Optimized Cubic Spline Method to Spheres

As discussed in section 2.6.6 the Optimized Cubic Spline Method gives the best results of the two previously developed methods (ELM and OCSM) in the case of cylinders. Therefore that method is applied to the sphere data. The range of data

obtained for the spheres is limited compared with that of the cylinders therefore the constraint placed on the final knot ($d_4 = d_3$ and $m_4 = m_3$) is not necessary here. Similar to the application of the OCSM to a cylinder, certain constraints on the optimization are necessary. This includes specifying that the s/d values at knot 1 are less than the s/d at knot 2, the s/d values at knot 2 are less than s/d at knot 3, etc. The s/d values are specified to be at least 0.05 apart although this limitation is not reached in the final result (i.e. the final knots are more than 0.05 apart). Another limitation placed on the optimization program is the value of the second knot (the first one inside the measured data) must be at least 0.04 from the beginning of the data. Again, this limitation is not reached in the final result (i.e. in the final result the knot is more than 0.4 from the beginning of the data).
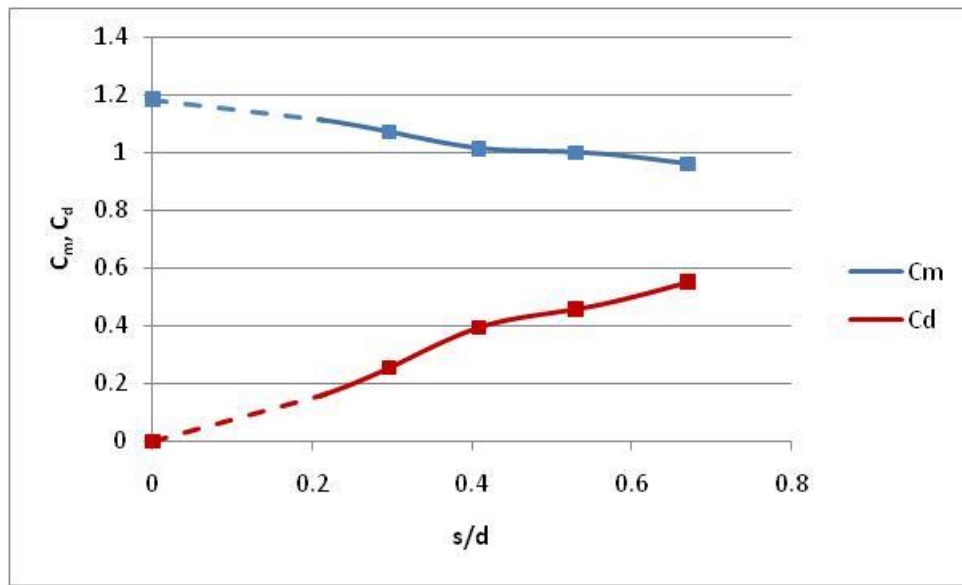
Figure 3.14: OCSM applied to sphere data (dotted line indicates extrapolated data, squares indicate the knot positions).

Applying the OCSM to the sphere data produces the results given in Figure 3.14. The added mass is seen to decrease while the unsteady drag increases. The added mass coefficient decreases more slowly than the unsteady drag increases. The initial value of the added mass was calculated to be 1.18. This is 18.4% higher than the expected value of 1, but it is within the range of the uncertainty. It also reflects the high initial values of

the original dimensionless force curves. It does, however, show that the value of C at the initial onset of acceleration is approximately 1.

Chapter 4 – Summary and Conclusions

This chapter first includes summaries of the two distinct sections of the dissertation, cylinder study and sphere study, followed by the conclusions.

4.1 Summary of Numerical Investigation of the Added Mass of Cylinders

A numerical model has been developed to determine details of the flow field in a fluid experiencing a unidirectional constant acceleration around a stationary cylinder. The force that is found using this model is used to determine the added mass of the object. Several features of the model are examined in order to produce the best possible simulation. These features included grid convergence, turbulence models, time sensitivity and three dimensional versus two dimensional simulations. The model is then compared to the experimental results of Sarpkaya and Garrison[13]. The largest difference between the two is found to be associated with the formation of a small secondary vortex just downstream of the flow separation point in the model results. Experimental flow visualization images of this case, available in the literature, do not indicate such a vortex. It is speculated that other experimental factors such as flow disturbances could be responsible for this discrepancy. The model, however, is considered to provide a reasonable tool for determining the forces on a cylinder subjected to unidirectional constant acceleration, especially in the initial stage. The results agree with the findings of others that the initial added mass is well predicted using potential flow.

The model is then used to investigate the effect on the added mass if the object started from some non-zero constant velocity, then accelerated in a unidirectional constant manner. In the first section of this work, a cylinder subjected to two different non-zero constant velocities followed by unidirectional constant acceleration is studied. These results are compared to the results for acceleration starting from rest (and Re = 0) as well as the available experimental results for that case. In order to make this comparison, Sarpkaya's dimensionless equation is generalized using kinematic values expressed relative to the time the acceleration is initiated. The new dimensionless

variables are capable of collapsing the numerical force results on one curve regardless of the initial constant velocity for the range of parameters studied.

The numerical experiments were repeated with a cylinder of the same diameter and initial non-zero constant velocity but with three different unidirectional constant accelerations. These results also are shown to collapse on the previous results when plotted non-dimensionally.

The final set of numerical experiments consists of simulating a cylinder with the same initial constant velocity and acceleration, however with three different diameters. Again, the results compare very well with the dimensionless experimental data.

Two methods for splitting the dimensionless force into the added mass coefficient and the unsteady drag coefficient are developed. The first method is referred to as the Equation of a Line Method or ELM. The basis for this method is the fact that the equation relating the dimensionless force, added mass, unsteady drag and the dimensionless displacement is linear. The slope of a line includes the unsteady drag coefficient and the added mass coefficient is included in the y intercept. The second method is referred to as the Optimization of a Cubic Spline Method or OCSM. This method utilizes two, five knot (three internal and two end knots) cubic splines. The first cubic spline approximates the added mass coefficient and the second cubic spline the unsteady drag coefficient. The positions of the knots are left as variables such that they could be changed in order to optimize the system using a method of least squares. This was accomplished by comparing the estimated dimensionless force (which is dependent on the combination of the two individual spline curves) with the actual dimensionless force.

The results of the two methods are compared with the force splitting results presented by Sarpkaya and Garrison[13] which is considered to be a good basis for comparison. It is determined that the OCSM gave better results therefore it is used for the remainder of the data analysis in this study including data from the numerical experiments.

4.2 Summary of Experimental Study of Added Mass of Spheres

A set of experiments is conducted to investigate the transient added mass and friction coefficient in the initial period of the release of a sphere in a stationary fluid. The experiments consisted of releasing a sphere from rest and recording the descent of the sphere using a high speed, high resolution video camera. Three different sets of spheres were chosen to give two different values of acceleration and a number of runs were conducted for each set.

The data are plotted using non-dimensional groups developed in a manner similar to that in the case of the circular cylinder. The resulting curves for the dimensionless force follow the same trends as those found in the cylinder work. The dimensionless total force is further analyzed in two ways. The first method uses the assumption that there is no drag which is exactly the case for constant acceleration. For this range the acceleration does not change more than 2% from its initial value. The second method includes the frictional term and the OCSM is used to separate the forces. The results demonstrate that the trend of the added mass and drag coefficients is similar to that found in the case of the circular cylinder and the added mass coefficient is close to the value determined by use of potential flow calculations.

4.3 Conclusions

The conclusions are grouped according to the natural division of the research into cylinders and spheres. Those associated with the work done with cylinders are first covered followed by the conclusions for the work done with spheres.

4.3.1 Cylinder Study

This study extends the knowledge base found in existing literature regarding the flow of fluid accelerated over a stationary cylinder in a unidirectional and constant manner and

the added mass. Computational fluid dynamics is used as a means of determining the force on a cylinder as well as its added mass. The following are the conclusions for this body of work.

1) A numerical model is developed that simulates, reasonably well, the flow of fluid with a unidirectional constant acceleration over a stationary cylinder.

2) Results of the numerical experiment conducted using the above mentioned model show that, regardless of initial velocity, acceleration or diameter, the data can be collapsed onto one curve by plotting dimensionless values based on the changes in displacement and velocity from those values at the time that the acceleration begins.

3) The dimensionless force determined for the case of constant non-zero velocity followed by unidirectional constant acceleration shows the same trend of starting at the potential flow value as the cylinder experiments that accelerated from rest.

4) The Equation of a Line Method of splitting the force into added mass and unsteady drag results in a curve that is similar in shape to the one based on vortex methods presented in the literature [13], however it does have differing values.

5) The Optimized Cubic Spline Method of splitting the force into added mass and unsteady drag is easier to implement than the vortex method [13] yielding similar trends in the curve as well as similar values. Although this technique requires more effort to apply than the ELM, it is the preferred technique because of the better agreement with the vortex technique.

4.3.2 Sphere Study

This study is different than previous studies on falling spheres in that the focus is on the added mass of the sphere. The results are related to and complement those of the

circular cylinder in that the added mass of the sphere is studied as it experiences an approximately constant and unidirectional acceleration. Techniques previously developed for analysis of the circular cylinder added mass are developed and applied in this case. The conclusions for this body of work are presented below.

1) The sphere falling from rest in a stationary fluid results in a similar trend in the dimensionless total force curve versus dimensionless distance as that of a circular cylinder. The value starts at approximately the value predicted by use of potential flow theory then rises with increasing slope over the range of this experiment.

2) The data analysis method that includes the assumption that there is no drag during the descent of the sphere results in an added mass that is reasonably close to the potential flow value. The difference is within the uncertainty of the experimental procedure.

3) The application of the Optimized Cubic Spline Method to the sphere data shows that the added mass is also reasonably close to the value of the potential flow value of added mass and decreases slightly with increasing s/d while the drag coefficient tends to zero initially and increases with increasing s/d. Again this is within the uncertainty of the experimental procedure.

Bibliography

1.   Du Buat, C., *Principles D'hydraulique*, Paris, 1786.

2.   Brennen, C.E., *A Review of Added Mass and Fluid Inertial Forces*, Report CR 82.010, Naval Civil Engineering Laboratory, Port Hueneme, California, 1982.

3.   Yih, C.S., *Fluid Mechanics: A Concise Introduction to the Theory*, McGraw-Hill New York, NY, 1969.

4.   Lamb, H., *Hydrodynamics*, *6th Ed.*, Dover Publications, New York, NY, 1945.

5.   Birkhoff, G., *Chapter 6: Added Mass*, in *Hydrodynamics: A Study in Logic, Fact and Similitude*, pp. 148-178, Princeton University Press, Princeton, New Jersey, 1960.

6.   Kennard, E., *Irrotational Flow of Frictionless Fluids : Mostly of Invariable Density*, Report 2299, David Taylor Model Basin, Washington, D.C., 1967.

7.   Patton, K.T., *Tables of Hydrodynamic Mass Factors for Translational Motion*, in *American Society of Mechanical Engineers - Meeting WA/UNT-2*, American Society of Mechanical Engineers (ASME), New York, NY, United States, 1965.

8.   Keulegan, G.H. and L.H. Carpenter, *Forces on Cylinders and Plates in Oscillating Fluid,* United States Bureau of Standards - Journal of Research, Vol. 60, pp. 423, 1958.

9.   Sarpkaya, T. and M. Isaacson, *Mechanics of Wave Forces on Offshore Structures*, Van Nostrand Reinhold Company, NY, 1981.

10.   Sarpkaya, T., *Lift, Drag, and Added-Mass Coefficients for Circular Cylinder Immersed in Time-Dependent Flow*, in *Journal of Applied Mechanics Meeting WA-61*, pp. 13-15, 1962.

11.   Villaggio, P., *The Added Mass of a Deformable Cylinder Moving in a Liquid,* Continuum Mechanics and Thermodynamics, Vol. 8, No. 2, pp. 115-120, 1996.

12.   Bird, A.R., *Measured Fluid Forces on an Accelerated/Decelerated Circular Cylinder (History Force)*, PhD Dissertation, *Department of Civil Engineering*, Northwestern University, Evanston, Illinois, 1984.

13.   Sarpkaya, T. and C.J. Garrison, *Vortex Formation and Resistance in Unsteady Flow,* Transactions of the ASME Journal of Applied Mechanics, pp. 16-24, March,1963.

14.   Garrison, C.J., *Resistance in Unsteady Flow*, M.A.Sc. Thesis, *Department of Engineering Mechanics*, University of Nebraska, Lincoln, Nebraska, 1962.

15.   Basset, A.B., *Hydrodynamics,* Philosophical Transactions, Vol. 2, pp. 43, 1888.

16.   Basset, A.B., *Descent of a Sphere in Viscous Liquid,* Nature, Vol. 83, pp. 369-381, 1910.

17.   Morison, J.R., M.P. O'Brien, J.W. Johnson, and S.A. Schaaf, *Force Exerted by Surface Waves on Piles,* American Institute of Mining and Metallurgical Engineers - Journal of Petroleum Technology, Vol. 2, No. 5, pp. 149-154, 1950.

18.   Hannoura, A.-A.A., *Numerical and Experimental Modelling of Unsteady flow in Rockfill Embankments*, PhD, *Department of Civil Engineering*, University of Windsor, Windsor, 1978.

19.   Hannoura, A.-A.A. and J.A. McCorquodale, *Rubble Mounds - Hydraulic Conductivity Equation,* Journal of Waterway Port Coastal and Ocean Engineering- ASCE, Vol. 111, No. 5, pp. 783-799, 1985.

20.   Hannoura, A.-A.A. and J.A. McCorquodale, *Virtual Mass of Coarse Granular Media,* Journal of the Waterway Port Coastal and Ocean Division - ASCE, Vol. 104, No. 2, pp. 191-200, 1978.

21.   Noca, F., *On the Evaluation of Time-Dependent Fluid Dynamic Forces on Bluff Bodies*, PhD Dissertation, *Graduate Aeronautical Labs*, California Institute of Technology, Pasedena, California, 1997.

22.   Noca, F., D. Shiels, and D. Jeon, *Measuring Instantaneous Fluid Dynamic Forces on Bodies, using only Velocity Fields and Their Derivatives,* Journal of Fluids and Structures, Vol. 11, pp. 345-350, 1997.

23.   Sarpkaya, T., *Forces on Cylinders and Spheres in a Sinusoidally Oscillating Fluid,* Journal of Applied Mechanics, Transactions ASME, Vol. 42, No. 1, pp. 32-37, 1975.

24.   Sarpkaya, T., *In-Line and Transverse Forces on Cylinders in Oscillatory Flow at High Reynolds Numbers,* Journal of Ship Research, Vol. 21, No. 1, pp. 200-216, 1977.

25.   Skop, R.A., S.E. Ramberg, and K.M. Ferer, *Added Mass and Damping Forces on Circular Cylinders,* American Society of Mechanical Engineers (Paper), No. 76, pp. 1-11, 1976.

26.   Cotter, D.C. and S.K. Chakrabarti, *Wave Force Tests on Vertical and Inclined Cylinders,* Journal of Waterway, Port, Coastal, and Ocean Engineering, Vol. 110, No. 1, pp. 1-14, 1984.

27.   Romagnoli, R. and R. Varvelli, *Drag and Added Mass Study on Arbitrarily Oscillating Marine Bodies*, in *Proceedings of the First (1990) European Offshore Mechanics Symposium*, Trondheim, Norway, Int Soc of Offshore and Polar Engineerns (ISOPE), 1990.

28.   Nakamura, M., K. Hoshino, and W. Koterayama, *Three-Dimensional Effects on Hydrodynamic Forces Acting on an Oscillating Finite-Length Circular Cylinder,* International Journal of Offshore and Polar Engineering, Vol. 2, No. 2, pp. 81-86, 1992.

29.   Hoshino, H., S. Kato, M. saito, and H. Sato, *Hydrodynamic Forces Acting on Finite-Length Circular Cylinder oscillating in a Uniform Flow*, in *Proceedings of the Third (1993) International Offshore and Polar Engineering Conference, Part 3 (of 4)*, Singapore, Singapore, Int Soc of Offshore and Polar Engineerns (ISOPE), 1993.

30.   Medeiros, E.F., *An Experimental Study of the Flow Structures and Hydrodynamic Forces of a Cylinder in a Reversing Flow*, PhD, The University of Texas at Austin, Austin, Texas, 1995.

31.   Dutsch, H., F. Durst, S. Becker, and H. Lienhart, *Low Reynolds-Number Flow Around an Oscillating Circular Cylinder at Low Keulegan-Carpenter Numbers,* Journal of Fluid Mechanics, Vol. 360, pp. 249-271, 1998.

32.   Nishihara, T., S. Kaneko, and T. Watanabe, *Characteristics of Fluid Dynamic Forces Acting on a Circular Cylinder Oscillated in the Streamwise Direction and its Wake Patterns,* Journal of Fluids and Structures, Vol. 20, No. 4, pp. 505-518, 2005.

33.   Odar, F. and W.S. Hamiltan, *Forces on a Sphere Accelerating in a Viscous Fluid,* Journal of Fluid Mechanics, Vol. 18, pp. 302-314, 1964.

34.   Abbad, M. and M. Souhar, *Effects of the History Force on an Oscillating Rigid Sphere at Low Reynolds Number,* Experiments in Fluids, Vol. 36, No. 5, pp. 775-82, 2004.

35.   Abbad, M., *Experimental Investigation on the History Force Acting on Oscillating Fluid Spheres at Low Reynolds Number,* Physics of Fluids, Vol. 16, No. 10, pp. 3808-3817, 2004.

36. Ikeda, Y., K. Osa, and N. Tanaka, *Viscous Forces Acting on Irregularly Oscillating Circular Cylinders and Flat Plates,* Journal of Offshore Mechanics and Arctic Engineering, Vol. 110, No. 2, pp. 140-147, 1988.

37. McConnel, K.G. and D.F. Young, *Added Mass of a Sphere in a Bounded Viscous Fluid,* ASCE - Journal of the Engineering Mechanics Division, Vol. 91, No. 4, pp. 147-164, 1965.

38. Chew, Y.T., H.T. Low, S.C. Wong, and K.T. Tan, *An Unsteady Wake-Source Model for Flow Past an Oscillating Circular Cylinder and its Implications for Morison's Equation,* Journal of Fluid Mechanics, Vol. 240, pp. 627, 1992.

39. Rahman, M. and D.D. Bhatta, *Evaluation of Added Mass and Damping Coefficient of an Oscillating Circular Cylinder,* Applied Mathematical Modelling, Vol. 17, No. 2, pp. 70-79, 1993.

40. Kim, I., S. Elghobashi, and W.A. Sirignano, *On the Equation for Spherical-Particle Motion: Effect of Reynolds and Acceleration Numbers,* Journal of Fluid Mechanics, Vol. 367, pp. 221-253, 1998.

41. Whitman, A.M., *Aspect Ratio Effects on the Added-Mass of a Slender Pulsating Cylinder,* Journal of Applied Mechanics, Vol. 39, No. 4, pp. 1047, 1972.

42. Mikishev, G.N. and V.I. Stolbetsov, *Vibrations of a Body in a Bounded Volume of Viscous Fluid,* Fluid Dynamics, Vol. 18, No. 1, pp. 12, 1983.

43. Keim, S.R., *Fluid Resistance to Cylinders in Accelerated Motion,* ASCE - Journal of the Hydraulics Division, Vol. 82, pp. 14, 1956.

44. Sarpkaya, T., *Separated Flow about Lifting Bodies and Impulsive Flow about Cylinders,* AIAA Journal, Vol. 4, No. 3, pp. 414, 1966.

45. McLain, T.W., *Modeling of Underwater Manipulator Hydrodynamics with Application to the Coordinated Control of an Arm/Vehicle System*, PhD Dissertation, *Department of Mechanical Engineering*, Stanford University, Stanford, California, 1995.

46. McLain, T.W. and S.M. Rock, *Experiments in the Hydrodynamic Modeling of an Underwater Manipulator,* Proceedings of the 1996 Symposium on Autonomous Underwater Vehicle Technology pp. 463-469, 1996.

47. Moorman, R.B., *Motion of a Spherical Particle in the Accelerated Portion of Free Fall*, PhD Dissertation, *Department of Mechanics and Hydraulics*, State University of Iowa, Iowa City, Iowa, 1955.

48. Odar, F., *Verification of the Proposed Equation for Calculation of the Forces on a Sphere Accelerating in a Viscous Fluid,* Fluid Mechanics, Vol. 25, No. 3, pp. 591-592, 1966.

49. Hamilton, W. and G. Courtney, *Added Mass of Sphere Starting Upward Near Floor,* ASCE J Eng Mech Div, Vol. 103, No. 1, pp. 79-97, 1977.

50. Wang, X. and C. Dalton, *Numerical Solutions for Impulsively started and Decelerated Viscous Flow Past a Circular Cylinder,* International Journal for Numerical Methods in Engineering, Vol. 12, pp. 383, 1991.

51. Ferreira, J.M. and R.P. Chhabra, *Accelerating Motion of a Vertically Falling Sphere in Incompressible Newtonian Media: an Analytical Solution,* Power Technology, Vol. 97, pp. 6-15, 1998.

52. Chang, T.-J. and B.C. Yen, *Gravitational Fall Velocity of Sphere in Viscous Fluid,* Journal of Engineering Mechanics, Vol. 124, No. 11, pp. 1193-1199, 1998.

53. Guo, J., *Motion of Spheres Falling Through Fluids,* Journal of Hydraulic Research, Vol. 49, No. 1, pp. 32-41, 2011.

54. Schlichting, H., *Boundary-Layer Theory*, *6th Ed.*, McGraw-Hill, New York, NY, 1968.

55. Kikuchi, K. and O. Mochizuki, *Consideration of Thrust in Escaping Motion of a Mosquito Larva,* Journal of Aero Aqua Bio-mechanisms, Vol. 1, No. 1, pp. 111-116, 2010.

56. Brennen, C.E., *Fundamentals of Multiphase Flow*, Cambridge University Press, Cambridge, England, 2005.

57. *Fluent User Manual Version 6.3.26*, Fluent Inc., Lebanon, NH, USA, 2006.

58. Jones, D.A. and D.B. Clark, *Simulation of a Wing-Body Junction Experiment using the Fluent Code*, DSTO-TR-1731, Report for Australian Department of Defence, Australia, 2005.

59. Anderson, J.D., *Fundamentals of Aerodynamics*, *3rd Ed.*, McGraw-Hill, Boston, 2001.

60. Munson, B.R., D.F. Young, and T. Okiishi, H., *Fundamentals of Fluid Mechanics*, *4th Ed.*, John Wiley & Sons, Inc., New York, NY,, 2002.

61. Chapra, S.C. and R.P. Canale, *Numerical Methods for Engineers*, *2nd Ed.*, McGraw-Hill, 1998.

62.   Coleman, H.W. and W.G. Steele, *Experimentation and Uncertainty Analysis for Engineers*, *2nd Ed.*, John Wiley & sons, 1999.

Appendix A – User Defined Function

The following is the user defined function used to control the velocity of the inlet boundary for the simulations described in Chapter 2.

```c
/*********************************************************************
  unsteady.c
  UDF for specifying a transient velocity profile boundary condition
*********************************************************************/

#include "udf.h"

DEFINE_PROFILE(un_accel9o81re0, thread, position)
{
  face_t f;
  real t = CURRENT_TIME;

/*********************************************************************
Velocity_init is the initial velocity of the flow  used for the constant portion of the
simulation.  This was calculated for the desired Reynolds number based on the diameter.

accelerationstart is the time that the acceleration starts.
*********************************************************************/
  begin_f_loop(f, thread)
   {
    F_PROFILE(f, thread, position) =Velocity_Init + (9.81*(t-accelerationstart));
   }
  end_f_loop(f, thread)
}
```

Appendix B – Uncertainty Analysis

There is a certain amount of uncertainty involved with any experimental measurement. The purpose of this appendix is to explore the uncertainty in the measurements used for the experiments involving the sphere.

B.1 Uncertainty for Gravitational Acceleration

Gravitational acceleration can be calculated based on the latitude and the height of the experimental location above sea level,

$$g = 9.78(1 + 5.3e^{-3}sin^2\phi - 5.8e^{-6}sin^2 2\phi) \\ -3.086e^{-6}h,$$ (B.1)

where ϕ is the latitude and h is the height above sea level.

The uncertainty in the gravitational acceleration can be expressed as

$$U_g = \sqrt{\left(\frac{\partial g}{\partial \emptyset}U_\emptyset\right)^2 + \left(\frac{\partial g}{\partial h}U_h\right)^2},$$ (B.2)

where,

$$\frac{\partial g}{\partial \emptyset} = 0.1037 \, sin\emptyset \, cos\emptyset - 1.134e^{-4} \sin 4\emptyset,$$ (B.3)

and

$$\frac{\partial g}{\partial h} = -3.086e^{-6}.$$ (B.4)

The uncertainty for the measurement of the latitude is $U_\emptyset = \pm 5e^{-3} \, rad$ and the uncertainty for the height is $U_h = \pm 1 \, m$.

For example for Windsor, Ontario, Canada $\emptyset = 42.3° = 0.738 \, rad$ and $h = 190 \, m$. Therefore Equation B.2 becomes,

$$U_g = \sqrt{\left(\left(\genfrac{}{}{0pt}{}{0.103718\ sin(0.738)\ cos(0.738)}{-1.13452\ e^{-4}sin(4 \times 0.738)}\right) \times 5e^{-3}\right)^2 + \left((-3.086e^{-6}) \times 1\right)^2} .$$

(B.5)

This results in,

$$U_g = \pm 2.58e^{-4}\ \frac{m}{s^2}.$$

(B.6)

B.2 Uncertainty for Weight minus Buoyancy Force

This section develops the uncertainty equations for the weight minus the buoyancy force. The equation can be expressed as

$$W - F_B = M_{inWater}g$$

(B.7)

where $M_{inWater}$ is the mass of the sphere suspended in water. The uncertainty can be expressed as

$$U_{W-F_B} = \sqrt{\left(\frac{\partial(W - F_B)}{\partial M_{inWater}}U_{M_{inWater}}\right)^2 + \left(\frac{\partial(W - F_B)}{\partial g}U_g\right)^2},$$

(B.8)

where,

$$\frac{\partial(W - F_B)}{\partial M_{inWater}} = g,$$

(B.9)

and

$$\frac{\partial(W - F_B)}{\partial g} = M_{inWater.}$$

(B.10)

Substituting Equation B.9 and B10 into Equation B.8 results in,

$$U_{W-F_B} = \sqrt{\left(gU_{M_{inWater}}\right)^2 + \left(M_{inWater}U_g\right)^2}. \tag{B.11}$$

For example, for sphere 3 $M_{inWater}$= 0.0263 kg, g = 9.80 m/s², $U_{M_{inWater}}$= ±0.000005 kg, and U_g = ±2.58 e⁻³ m/s². Equation B.11 becomes,

$$U_{W-F_B} = \sqrt{\begin{array}{l} \left(9.80\dfrac{m}{s^2}(0.000005\ kg)\right)^2 \\ + \left(0.0263\ kg\ \left(2.58\ e^{-4}\dfrac{m}{s^2}\right)\right)^2 \end{array}}. \tag{B.12}$$

This results in,

$$U_{W-F_B} = \pm 4.95\ e^{-5}N. \tag{B.13}$$

B.3 Uncertainty for M$_{add, the}$ (theoretical added mass)

This section develops the uncertainty equations for the calculating the theoretical added mass. The equation for the theoretical added mass is,

$$M_{add,the} = \frac{2}{3}\pi r^3 \rho = \frac{1}{2}V\rho. \tag{B.14}$$

The uncertainty for the added mass can be expressed as,

$$U_{M_{add,the}} = \sqrt{\left(\frac{\partial M_{add,the}}{\partial r}U_r\right)^2 + \left(\frac{\partial M_{add,the}}{\partial \rho}U_\rho\right)^2}. \tag{B.15}$$

The uncertainty in the radius was obtained from the manufacturer,

$$U_r = \frac{U_d}{2} = \frac{0.001\ in}{2} = 0.0005\ in\ \times \frac{0.0254\ m}{1\ in} = 1.27e^{-5}m. \tag{B.16}$$

The uncertainty for the density is taken to be

$$U_\rho = \pm 1 \, \frac{kg}{m^3}. \tag{B.17}$$

The partial differentials in Equation B.15 can be calculated as,

$$\frac{\partial M_{add,the}}{\partial r} = 2\pi r^2 \rho, \tag{B.18}$$

and

$$\frac{\partial M_{add,the}}{\partial \rho} = \frac{2}{3} \pi r^3. \tag{B.19}$$

Substituting Equation B.18 and B.19 into Equation B.15, the uncertainty in the theoretical added mass can be expressed as

$$U_{M_{add,the}} = \sqrt{(2\pi r^2 \rho U_r)^2 + \left(\frac{2}{3}\pi r^3 U_\rho\right)^2} \tag{B.20}$$

For example, the uncertainty in the theoretical added mass for a sphere with a diameter of 0.0254 m (1 inch) in water at 20°C is,

$$U_{M_{add,the}} = \sqrt{ \begin{array}{c} \left(2\pi \left(\frac{0.0254\ m}{2}\right)^2 \left(998.2 \frac{kg}{m^3}\right)(1.27e^{-5}m)\right)^2 \\[2ex] + \left(\frac{2}{3}\pi \left(\frac{0.0254\ m}{2}\right)^3 \left(1\frac{kg}{m^3}\right)\right)^2 \end{array} }. \tag{B.21}$$

The result is,

$$U_{M_{add,the}} = \pm 1.354e^{-5} \text{ kg.} \tag{B.22}$$

B.4 Uncertainty in Determining C using Curve Fits for Acceleration

This section begins with the calculations for the uncertainty of the second order coefficient of the curve fit. This is then used to find the uncertainty of the acceleration.

B.4.1 Curve Fit Equations

The method of least squares was used to determine the second order polynomial curve fit for sets of 70 data points. The second order coefficient was then used to determine the acceleration for that set of data. The method of least squares starts with the equation

$$y = a_o + a_1 x_i + a_2 x_i^2. \tag{B.23}$$

The coefficients are determined by minimizing the sum of the square of the residuals. The residuals are expressed as

$$\in = y_i - y. \tag{B.24}$$

Substituting Equation B.23 into Equation B.24 gives,

$$\in = y_i - (a_o + a_1 x_i + a_2 x_i^2). \tag{B.25}$$

Simplifying Equation B.25 gives,

$$\in = y_i - a_o - a_1 x_i - a_2 x_i^2. \tag{B.26}$$

The sum of the squares of the residuals (Equation B.26) is,

$$S = \sum_{i=1}^{n} (y_i - a_o - a_1 x_i - a_2 x_i^2)^2. \tag{B.27}$$

In order to minimize the error, the derivative of each equation is taken with respect to each of the unknown coefficients of the polynomial,

$$\frac{\partial S}{\partial a_0} = \sum_{i=1}^{n} -2 (y_i - a_o - a_1 x_i - a_2 x_i^2) = 0, \tag{B.28}$$

86

$$\frac{\partial S}{\partial a_1} = \sum_{i=1}^{n} -2\,(y_i - a_o - a_1 x_i - a_2 x_i^2)x_i = 0, \tag{B.29}$$

$$\frac{\partial S}{\partial a_2} = \sum_{i=1}^{n} -2\,(y_i - a_o - a_1 x_i - a_2 x_i^2)x_i^2 = 0. \tag{B.30}$$

Rearranging the equations B.28-B.30 gives,

$$a_0 + a_1 \sum_{i=1}^{n} x_i + a_2 \sum_{i=1}^{n} x_i^2 = \sum_{i=1}^{n} y_i, \tag{B.31}$$

$$a_0 \sum_{i=1}^{n} x_i + a_1 \sum_{i=1}^{n} x_i^2 + a_2 \sum_{i=1}^{n} x_i^3 = \sum_{i=1}^{n} y_i\,x_i, \tag{B.32}$$

$$a_0 \sum_{i=1}^{n} x_i^2 + a_1 \sum_{i=1}^{n} x_i^3 + a_2 \sum_{i=1}^{n} x_i^4 = \sum_{i=1}^{n} y_i x_i^2. \tag{B.33}$$

This results in a set of linear equations in which the variables a_o, a_1, and a_2 are the desired quantities for which a solution is required. Using Matlab to solve the linear system equations gives the following relations between the coefficients and the summations for the set of 70 data points;

$$a_0 = \frac{\sum x_i^2 \sum x_i^4 \sum y_i - \sum x_i^2 \sum x_i^2 \sum y_i x_i^2 + \sum x_i^2 \sum x_i^3 \sum y_i x_i - \sum x_i^3 \sum x_i^3 \sum y_i - \sum x_i \sum x_i^4 \sum y_i x_i + \sum x_i \sum x_i^3 \sum y_i x_i^2}{\sum x_i^4 \sum x_i^2 - \sum x_i^4 \sum x_i \sum x_i - \sum x_i^2 \sum x_i^2 \sum x_i^2 - \sum x_i^3 \sum x_i^3 + \sum x_i^3 \sum x_i \sum x_i^2 + \sum x_i^2 \sum x_i \sum x_i^3}, \tag{B.34}$$

$$a_1 = \frac{\sum x_i^4 \sum y_i x_i - \sum x_i^2 \sum x_i^2 \sum y_i x_i - \sum x_i \sum x_i^4 \sum y_i - \sum x_i^3 \sum y_i x_i^2 + \sum x_i^2 \sum x_i^3 \sum y_i + \sum x_i \sum x_i^2 \sum y_i x_i^2}{\sum x_i^4 \sum x_i^2 - \sum x_i^4 \sum x_i \sum x_i - \sum x_i^2 \sum x_i^2 \sum x_i^2 - \sum x_i^3 \sum x_i^3 + \sum x_i^3 \sum x_i \sum x_i^2 + \sum x_i^2 \sum x_i \sum x_i^3}, \tag{B.35}$$

$$a_2 = \frac{\sum x_i^2 \sum y_i x_i^2 - \sum x_i \sum x_i \sum y_i x_i^2 - \sum x_i^2 \sum x_i^2 \sum y_i - \sum x_i^3 \sum y_i x_i + \sum x_i \sum x_i^3 \sum y_i + \sum x_i \sum x_i^2 \sum y_i x_i}{\sum x_i^4 \sum x_i^2 - \sum x_i^4 \sum x_i \sum x_i - \sum x_i^2 \sum x_i^2 \sum x_i^2 - \sum x_i^3 \sum x_i^3 + \sum x_i^3 \sum x_i \sum x_i^2 + \sum x_i^2 \sum x_i \sum x_i^3}.$$

$$(B.36)$$

Since the coefficient a_2 is related to acceleration, the uncertainty for this coefficient will be needed.

B.4.2 Uncertainty in Acceleration

The uncertainty for the second order coefficient of the curve fit will be used to determine the uncertainty of the acceleration. Equation B.36 can be considered a data reduction equation of the form

$$a_2 = \frac{a}{2} = a_2\,(x_1, x_2, \ldots, x_n, y_1, y_2, \ldots, y_n), \qquad (B.37)$$

where $x_1, x_2, \ldots, x_n$ are the times in seconds for each of the 70 data points used for each curve fit and $y_1, y_2, \ldots, y_n$ are the displacements in m for each of the 70 data points used for each curve fit (this equation will only give the uncertainty for one point on the acceleration curve). Applying the uncertainty analysis equations (Coleman and Steele[62] 1999) to equation B.36, the general form of uncertainty is

$$U_{a_2}^2 = \sum_{i=1}^{n} \left(\frac{\partial a_2}{\partial y_i}\right)^2 P_{y_i}^2 + \sum_{i=1}^{n} \left(\frac{\partial a_2}{\partial y_i}\right)^2 B_{y_i}^2 + \sum_{i=1}^{n} \left(\frac{\partial a_2}{\partial x_i}\right)^2 B_{x_i}^2, \qquad (B.38)$$

where P_y is the random uncertainty variable (the uncertainty associated with the goodness of the curve fit) for the y, B_y is the systematic uncertainty (the uncertainty associated with the experimental measurement) for the y variable and B_x is the systematic uncertainty for the x variable. It is assumed that there is no random uncertainty in x.

P_y can be obtained from the curve fits in Excel. The systematic uncertainty for the y variable (which is displacement) can be determined by the following equation, applied to the displacement data,

$$B_{y_i}^2 = (S_y)^2,$$ (B.39)

where,

$$S_y = \sqrt{\frac{1}{n-1}\sum_{i=1}^{n}(y_i - \bar{y})^2}.$$ (B.40)

One standard deviation was used for these calculations. The partial differentiation of a_2 is needed with respect to y_i and x_i. Equation A.36 is a complicated combination of small functions of $\sum y_i$ and $\sum x_i$. With this in mind the partial differentiation was done using a combination of the quotient rule and the product rule

$$\sum \left(\frac{\partial a_2}{\partial y_i}\right)^2 = \sum \left(\frac{\partial a_2}{\partial y_1} + \frac{\partial a_2}{\partial y_2} + \cdots + \frac{\partial a_2}{\partial y_i}\right)^2$$ (B.41)

Remember

$$a = 2a_2.$$ (B.42)

Therefore,

$$U_a = \sqrt{\left(\frac{\partial a}{\partial a_2} U_{a_2}\right)^2}.$$ (B.43)

The partial differential of acceleration with respect to a_2 is

$$\frac{\partial a}{\partial a_2} = 2.$$ (B.44)

89

Substituting Equation B.44 into Equation B.43 results in,

$$U_a = \sqrt{\left(2U_{a_2}\right)^2}.$$

(B.45)

Simplifying Equation B.45 gives,

$$U_a = 2U_{a_2}.$$

(B.46)

This is the uncertainty in one value of acceleration (one s/d) for one run. Since each ball consisted of multiple runs the average acceleration for all runs can be expressed as

$$a_{avg} = \frac{a_{r1} + a_{r2} + \cdots + a_{rn}}{n}.$$

(B.47)

The uncertainty in a_{avg} can be expressed as

$$U_{a_{avg}} = \sqrt{\left(\frac{\partial a_{avg}}{\partial a_{r1}} U_{a_{r1}}\right)^2 + \left(\frac{\partial a_{avg}}{\partial a_{r2}} U_{a_{r2}}\right)^2 + \cdots + \left(\frac{\partial a_{avg}}{\partial a_{rn}} U_{a_{rn}}\right)^2}.$$

(B.48)

Simplifying Equation B.48,

$$U_{a_{avg}} = \sqrt{\left(\frac{1}{n} U_{a_{r1}}\right)^2 + \left(\frac{1}{n} U_{a_{r2}}\right)^2 + \cdots + \left(\frac{1}{n} U_{a_{rn}}\right)^2}.$$

(B.49)

If the values for the uncertainties for each run are assumed to be approximately the same, then Equation B.49 becomes,

$$U_{a_{avg}} = \sqrt{n \left(\frac{1}{n} U_{a_r}\right)^2}.$$

(B.50)

where U_{a_r} is the average value of the uncertainties.

For example, the acceleration uncertainty for sphere 3 for the first four runs are

$U_{a_{r1}} = \pm 0.2230 \frac{m}{s^2}, U_{a_{r1}} = \pm 0.2230 \frac{m}{s^2}, U_{a_{r1}} = \pm 0.2215 \frac{m}{s^2}, U_{a_{r1}} = \pm 0.2235 \frac{m}{s^2}.$

These values are very close to the average value of $U_{a_r} = 0.1690$ m/s^2 Equation B.50 then becomes,

$$U_{a_{avg}} = \sqrt{28\left(\frac{1}{28}0.1690\right)^2}.$$

(B.51)

The result is

$$U_{a_{avg}} = \pm 0.0319\frac{m}{s^2}.$$

(B.52)

B.4.3 Uncertainty in C

The equation used to determine C for the sphere is

$$\left[\frac{W - F_B}{a_{avg}} - M\right]\frac{1}{M_{add,the}} = C.$$

(B.53)

The uncertainty for C can be expressed as

$$U_C = \sqrt{\begin{array}{l}\left(\dfrac{\partial C}{\partial(W - F_B)}U_{W-F_B}\right)^2 + \left(\dfrac{\partial C}{\partial a_{avg}}U_{a_{avg}}\right)^2 \\ + \left(\dfrac{\partial C}{\partial M}U_M\right)^2 + \left(\dfrac{\partial C_A}{\partial M_{add,the}}U_{M_{add,the}}\right)^2\end{array}}.$$

(B.54)

The partial differentials can be expressed as,

$$\frac{\partial C}{\partial(W - F_B)} = \frac{1}{a_{avg}M_{add,the}},$$

(B.55)

$$\frac{\partial C}{\partial a_{avg}} = -\frac{W - F_B}{a_{avg}^2 M_{add,the}},$$

(B.56)

$$\frac{\partial C}{\partial M} = \frac{1}{M_{add,the}}, \tag{B.57}$$

$$\frac{\partial C_A}{\partial M_{add.the}} = \frac{a_{avg}M - (W - F_B)}{M_{add,the}^2 a_{avg}}. \tag{B.58}$$

Substituting Equation B.55-B.58 into Equation B.54 gives,

$$U_C = \sqrt{\begin{array}{l} \left(\dfrac{1}{a_{avg}M_{add,the}}U_{W-F_B}\right)^2 \\ + \left(-\dfrac{W - F_B}{a_{avg}^2 M_{add,the}}U_{a_{avg}}\right)^2 \\ + \left(\dfrac{1}{M_{add.the}}U_M\right)^2 \\ + \left(\dfrac{a_{avg}M - (W - F_B)}{M_{add,the}^2 a_{avg}}U_{M_{add.the}}\right)^2 \end{array}} \tag{B.59}$$

For example, using the information from sphere 3, the uncertainty at t = 0.037 s can be calculated using the following values, a_{avg}=8.026 m/s^2, M$_{add,the}$ =1.806 e^{-3} kg, W-F$_B$ = 0.264196 N, M = 0.03066 kg, $U_{a_{avg}} = \pm 0.0319 \frac{m}{s^2}$, $U_{M_{add,the}} = \pm 1.354e^{-5} \, kg$, $U_{W-F_B} = \pm 4.95e^{-5} \, N$, U$_M$ = $\pm$ 0.000005 kg,

$$U_C = \sqrt{\begin{array}{l} \left(\dfrac{1}{8.026\frac{m}{s^2}\,(1.806e^{-3}\,kg)}\,(4.95e^{-5}\,N) \right)^2 \\[2em] + \left(-\dfrac{0.264196\,N}{\left(8.026\frac{m}{s^2}\right)^2 (1.806e^{-3}\,kg)}\,\left(0.0319\frac{m}{s^2}\right) \right)^2 \\[2em] + \left(\dfrac{1}{(1.806e^{-3}\,kg)}\,(0.000005\,kg) \right)^2 \\[2em] + \left(\dfrac{8.026\frac{m}{s^2}\,(0.03066\,kg) - (0.264196\,N)}{(1.806e^{-3}\,kg)^2\left(8.026\frac{m}{s^2}\right)}\,(1.354e^{-5}\,kg) \right)^2 \end{array}} \tag{B.60}$$

The results is

$$U_C = 0.1548. \tag{B.61}$$

This is the uncertainty for on standard deviation which includes 66.6% of the data. Two standard deviations will be used in order to include 95% of the data. This results in an uncertainty in the calculation of C,

$$U_{C_{2\sigma}} = 0.3098. \tag{B.62}$$

B.5 Uncertainty in s/d

The dimensionless distance can be represented by the equation

$$\text{Dimensionless distance} = s_{avg}/d \tag{B.63}$$

where s_{avg} is the average distance at a given time. The uncertainty for each distance measurement in each run is the same. Therefore the uncertainty for the average can be given by

$$U_{S_{avg}} = \sqrt{n\left(\frac{1}{n}U_{s_r}\right)^2} \qquad (\text{B.64})$$

where the uncertainty for one distance measurement is ±1 pixel. For sphere 3 1pixel = 3.570e^{-5} m therefore $U_{s_r} = \pm3.570$e^{-5} m and there are 28 runs (n = 28). Therefore Equation B.64 becomes

$$U_{S_{avg}} = \sqrt{28\left(\frac{1}{28}3.570e^{-5}\ m\right)^2}. \qquad (\text{B.65})$$

The result is,

$$U_{S_{avg}} = \pm6.748e^{-6}\ m. \qquad (\text{B.66})$$

The uncertainty in the dimensionless distance can be expressed as

$$U_{S_{avg}/d} = \sqrt{\left(\frac{\partial\left(s_{avg}/d\right)}{\partial s_{avg}}U_{S_{avg}}\right)^2 + \left(\frac{\partial\left(s_{avg}/d\right)}{\partial d}U_d\right)^2}, \qquad (\text{B.67})$$

where

$$\frac{\partial\left(\frac{S_{avg}}{d}\right)}{\partial s_{avg}} = \frac{1}{d}, \qquad (\text{B.68})$$

and

$$\frac{\partial\left(\frac{S_{avg}}{d}\right)}{\partial d} = -\frac{S_{avg}}{d^2}. \qquad (\text{B.69})$$

Substituting Equation B.67 and B.68 into Equation B.67 gives,

$$U_{S_{avg}/d} = \sqrt{\left(\frac{1}{d}U_{S_{avg}}\right)^2 + \left(-\frac{S_{avg}}{d^2}U_d\right)^2}. \tag{B.70}$$

For sphere 3 the manufacturer specifications of the uncertainty for the diameter of the sphere is ±0.0005 in = ± 0.0000127 m, the diameter of the sphere is 0.01905 m, the average distance at time = 0.037 s is 0.0058 m and the uncertainty for the average distance is ±6.748 e^{-6} m. Equation B.70 becomes

$$U_{S_{avg}/d} = \sqrt{\begin{array}{c}\left(\frac{1}{0.01905\ m}6.748e^{-6}m\right)^2 + \\ \left(-\frac{0.0058\ m}{(0.01905\ m)^2}0.0000127\ m\right)^2\end{array}}. \tag{B.71}$$

The result is

$$U_{S_{avg}/d} = 4.083e^{-4} \tag{B.72}$$

Similar to the uncertainty for the dimensionless force this is for one standard deviation. Therefore in order to get two standard deviations Equation B.72 must be multiplied by 2,

$$U_{S_{avg}/d_{2\sigma}} = 8.166e^{-4} \tag{B.73}$$

Vita Auctoris

Name: Shelagh A. Fackrell

Place of Birth: Windsor, Ontario

Year of Birth: 1976

Education: University of Windsor, Windsor, Ontario
                    1994-1998, B.A.Sc.

                    University of Windsor, Windsor, Ontario
                    1999-2001, M.A.Sc.

                    University of Windsor, Windsor, Ontario
                    2002-2011, Ph.D. (candidate)